The final publication is available at

https://doi.org/10.1016/j.applthermaleng.2021.117884

Additional Information

Thermal runaway evaluation and thermal performance enhancement of a lithium-ion battery coupling cooling system and battery sub-models

Antonio García*, Javier Monsalve-Serrano, Rafael Lago Sari, Santiago Martinez-Boggio

CMT - Motores Térmicos, Universitat Politècnica de València, Camino de Vera s/n, 46022 Valencia, Spain

Corresponding author (*):

Dr. Antonio García Martínez (angarma8@mot.upv.es)

Phone: +34 963876574

Abstract

This paper presents a novel simulation approach consisting of coupling fundamental and applicate aspects of Lithium-Ion battery simulations. A battery module representative of a complete battery pack is built using GT-AutoLion, consisting of a detailed electrochemical model and detailed cooling system modelled using the finite elements approach. The results show fresh and aged cylindrical cells submitted to different battery cooling flows. The cells are charged and discharged in high C_{rates} to observe the performance of the proposed system in critical conditions. In addition, a battery thermal runaway code in Python is coupled to simulate the decomposition of the main components of the battery cell and their associated heat release during the battery operation. The concentration of the main species is tracked as well as the battery cells temperature distribution. The aged cells shown more probabilities of thermal runaway due to the increase of the internal resistance. However, it is possible to reduce the difference by increasing the cooling flow from 3 g/s to 50 g/s. When analysing the thermal runaway induced by a failure of a cell, the comparison shows that the mechanisms found in the bibliography shows a difference of 40 seconds in predicting the peak of heat release rate. Overall, the proposed framework confirms its capability of addressing the relevant phenomena during the battery operation, providing a way of improving the design phase from the battery cell to the battery pack.

Keywords

Battery Thermal Runaway; Chemical Kinetics; Heat Transfer; Vehicle Safety

1. Introduction

Different outlooks suggest that the passenger cars energy vectors will change significantly in the next years [1] [2]. Battery electric vehicles (BEVs) will increase their market share if the legislation continues to be based on tailpipe emissions, since BEVs are zero CO_2 tailpipe emissions [3]. Technologies such as efficiently gasoline engines [4][5] or hydrogens solutions [6] are losing interest. One of the most important devices in BEVs and HEVs is the battery, which is responsible of the energy storage. State-of-the-art energy storage system are mainly composed by lithium-ion cells, which are arranged in parallel and series connection to attain high voltage (>600 V) and high energy content (>40 kWh) [7]. Depending on the configuration, there are three types of battery cells: cylindrical, prismatic and pouch cells [8]. These three types of cells can be found in commercial vehicles (energy density >100 Wh/kg) [9].

Compared to other rechargeable battery technologies, Lithium-Ion batteries have superior features such as high power and specific energy, low self-discharge rate, and long lifetime. However, the cycle life, performance, and safety of Lithium-ion batteries are highly dependent on the working temperature [10]. The proper temperature range for the operation of a Lithium-ion battery is between 25°C and 40°C and the maximum temperature difference between the modules in a battery pack should be less than 5°C [11]. If the cell overpasses 80°C, an irreversible damage is generated with a notable loss in performance. At high temperatures (>120°C), the decomposition of the solid electrolyte interface (SEI) decomposition may lead to an internal short-circuit, originating a phenomena called battery thermal runaway (BTR) [12]. In addition, the cell balance in a battery package is crucial to reduce the load unbalance [13]. Thermal runaway is a widely observed phenomenon in chemical and combustion processes, referring to an overheating event in which exothermic chain reactions take place originating a dangerous and destructive process [14]. Failure of the battery may then be accompanied by the release of toxic gas, fire, jet flames, and explosion [15]. Once the onboard battery is on fire, there is a great difficulty in suppressing it, because the burning battery pack is inaccessible to externally applied suppressant and can re-ignite without sufficient cooling. The review from Sun et al. [16] shows that the common causes of EV fires include the self-ignition (or spontaneous/auto ignition) in parked vehicles due to arson or sustained abuse, fire during the charging process, self-ignition while in driving, and fire after the traffic accident such as the high-speed collision. In this review, 16 BEV fire accidents were collected, where 62% happened while the car was parked and more than the half of these vehicles when charging. Therefore, the development of safety strategies and the correct coupling between the different degradation mechanisms that may lead to the BTR phenomenon are of utmost importance [17].

Controlling the battery temperature may offer a path to avoid the occurrence of thermal runaway induced by thermal abuse, the major contributor to the BTR events [18]. For the temperature control of the battery cell, a dedicated cooling system is used in commercial applications. They are categorized based on their objective (only cooling, or

cooling and heating), method (passive, where only the ambient environment is used, or active cooling, where a built-in source is utilized for heating/cooling), and heat transfer medium (air distributed or liquid via direct/indirect contact) [19]. Jiaqiang et al. [24][20] studied the effect of the inlet airflow velocity, air inlet radius, inlet and outlet eccentricity, and air vent area ratio in a battery pack with air cooling. Air vent area ratio, eccentricity and the inlet airflow velocity have the most significant effect on average temperature, temperature difference and heat conduction coefficient of power lithium-ion battery pack, respectively. Active liquid cooling with heating capabilities in indirect way is one of the most common battery thermal management system in BEVs due to the high cooling efficiency, compact structure, and flexibility to be applied in different environments [21]. It has been applied in numerous EVs on the market, such as Tesla Model S and Model 3, Chevrolet Volt, Chevrolet Bolt, and Audi e-Tron [22]. Several studies showed the effects of different battery cooling systems in normal cell operation range. Monika et al. [23] studied the pouch cell with mini-channels with 3D CFD approach at different ambient temperatures and constant discharge rates. The size and number of the mini-channels, mass flow and coolant inlet temperature were changed at constant discharge rate (3 C_{rate}). A cold plate comprising a total number of 5 mini-channels each of 6 mm width, and water as the coolant at an entry temperature of 25 °C with the mass flow rate of 3 g/s was found ideal for maintaining the temperature of the 20 Ah pouch cell battery module within a desirable range of 25°C and 40°C for any climatic conditions. Guo et al. [24] studied a refrigerant-based temperature management systems (TMS) for BEVs aiming to understand the interplay between the cabin thermal comfort and the battery thermal safety. The results show that both the temperatures of the cabin air and the battery pack can be well controlled. The energy consumption of this system decreases with the number of consecutive cycles. The TMS consumption accounts for 19.2% of the total consumption during the first driving cycle but decreases to 9.3% during the third driving cycle. The phase change material (PCM) based battery thermal management system is another effective cooling system for ensuring the reliability, safety, lifespan and performance of li-ion batteries [25]. However, the maturity and cost of this technology need to be further investigated [26].

Despite the cooling capacity in controlling the temperature of the cell, thermal runaway related issues are frequently reported, becoming a major safety concern for HEVs and BEVs [27]. Limit conditions such as high charge and discharge current, aged cells and high environment temperatures may provide enough heat generation to achieve the required energy of activation of the decomposition reactions. In this sense, not only the heat generation from Joule effect should be considered in battery design phase but also the degradation of the cell as well as the associated heat from the degradation reactions. Regardless of the relevance of these effects, only a few studies use multi-physics to deal with the coupling of cooling, electrochemical and thermal issues that may occurs during the battery utilization. Katrasnik et al. [14] presented an advanced multi-scale battery modelling framework that can be seamlessly integrated into multi-domain models. The modelling approach is based on the continuous modelling approach featuring more consistent virtual representation of the electrode topology and incorporating the

coupled chain of models for heat generations and side reactions. Moreover, Feng et al. [28] show a coupled electrochemical-thermal BTR model for Lithium-Ion batteries, allowing to simultaneously predict the voltage and temperature during the BTR. However, both approaches are used in an isolated cell without accounting the battery-module interaction. In addition, they are dependent of a single thermal degradation mechanism, without accounting for the specificities of the battery cell cathode chemistry [29]. Current battery models are thus not yet capable of providing full answers to the interplay between electric and thermal boundary conditions, cell design and applied materials, side reactions and safety implications of batteries. Zuo et al. [30] presented a coupled electrochemical-thermal model to obtain the voltage, current, and temperature characteristics during battery discharging process and provide simulation data for SOC estimation. The experimental results and simulation results show a good agreement and maximum surface temperature errors at the test point under 0.5 C and 1.0 C discharging rate are 1.08 K and 0.95 K, respectively.

Based on the above literature review, the development of a closed framework able to deal with the different mechanisms that may affect battery operation and consequent battery failure prediction are still to be developed. Most of the previous research on liquid cooling active system has been focused on normal operative conditions and the integration in the vehicle. Therefore, this research aims at developing a novel framework for Lithium-Ion battery package design and the thermal runaway evaluation. With focus in contemplate fundamental an application basis. By addressing these concerns, this paper aims to add to the bibliography an improved framework capable to simulate Lithium-Ion batteries in normal and abuse conditions. This is achieved by including different sub-models, able to include a detailed and predictive description of phenoma such as cooling, electrochemical operation, and thermal degradation. It is important to note that the term BEV usually refers to road vehicles, but this approach can be applied to rail vehicles, surface and underwater vessels, and aerospace applications. Therefore, the paper can have an impact in the new energy storage generations.

2. Modelling framework

This study is developed considering the coupling of different simulation approaches, creating a complete framework for the battery evaluation in terms of cell, module (arrange of cells), and complete package (arrange of modules). This section aims at defining the object of study, the relevant information for each one of the modelling approaches such as the equations, validations and coupling strategy.

2.1. Battery cell specifications

For this study, Samsung INR18650-20R cells were used (the nomenclature is due to the cell diameter = 18 mm, length = 65 mm and 0 for being a cylindrical cell) with main characteristics presented in Table 1. The chemistry of the cathode is Lithium-Ion Nickel Rechargeable (INR) with a nomenclature: $LiNiMnCoO_2$. This type of cell is also referred as Nickel-Manganese-Cobalt oxide (NMC) hybrid chemistry, which has as advantage an increased energy capacity compared to Lithium Cobalt Oxide (LCO) and Lithium Iron Phosphate ($LiFePO_4$, LFP) chemistries. The anode is composed of graphite as most of the

lithium-ion cell of the market. The cell is well known for having high specific energy thanks to its energy dense NMC chemistry. This battery boasts a 2 Ah capacity which provides 198 Wh/kg. The voltage fully charged is 4.2V and the cut off voltage (minimum safety voltage) is 2.5 V. The selected batteries have a low internal resistance and long-life cycle, offering long storage life of three months or more. Standard charge for this battery is 180 min (100 mA cut-off). Rapid charge is 50 min at 25°C (100 mA cut-off).

Table 1 – Main Lithium-Ion Samsung 20R battery cell properties.

Parameter	Value
Cell format	18650
Cathode Chemistry	INR (LiNiMnCoO2)
Dimensions [mm]	18.3 x 65.0
Weight [g]	42.4
Nominal Voltage [V]	3.6
Nominal Capacity [Ah]	2.0
Current Charge Continuous/Peak [A]	1.0/4.0
Current Discharge Continuous/Peak [A]	22.0/30.0A
Total Energy [Wh]	8.4
Vent Cap holes	3
Voltage at 100% SOC [V]	4.2
Cut-off voltage [V]	2.5
Temperature use Range [℃]	-20 to 60

2.2. Lithium-Ion Battery model

The operation of a Lithium-ion battery is subject to different operating conditions which depend on the environment and requirements of the application. For example, the battery can be exposed to the winter of Norway (<10°C) or the warm weather of Death Valley in California (>40°C). In addition, the battery pack can be charged with high C_{rate} (>10) or slowly discharged in an urban driving cycle for a high energy pack (<0.05). On the other hand, the cycling of the cell also has significant impact on its performance [31]. The combination of these factors can result in several negative consequences such as the lithium plating, SEI growing or the material decomposition, which are known as degradation mechanisms [32]. Consequently, the battery cell is more likely to produce fails which can comprehend from increases in the resistance and capacity loss to complete failure by means of thermal runaway. A summary of some of the phenomena that takes place in a battery cell is presented in Figure 1.
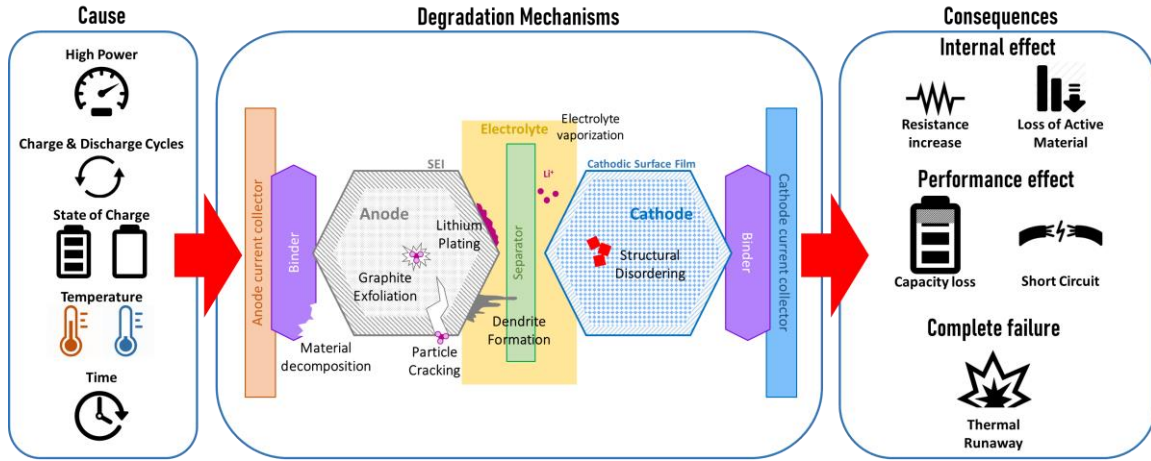
Figure 1- Scheme of thermal runaway cause and effects with the degradation mechanism in a Lithium-Ion cell.

Therefore, a coupled numerical approach is required to account the interplay of these phenomena and their influence on battery performance and safety. The individual modelling as well as the coupling framework of the important aspects of the battery cell is presented in the next subsections.

2.2.1. Electrochemical model

Charge conservation in the solid and electrolyte phases

The electric charge has a conservative nature, allowing to build transport equations that fulfil this constraint. In an electrochemical system, both the species and charge are conserved. The AutoLion defines a 2D electrochemical model for Lithium-ion (Li-ion) batteries based on the work of John Newman [33]. The main governing equations for a two-scale analysis of Li-ion battery cells is detailed below. For more information about all the involved equation see the work of Salvadori et al. [34]. Considering a separate layer with a solid electrode in one side and a liquid electrolyte in the other, the charge conservation equation for the solid phase can be represented by Equation 1:

$$0 = \frac{\partial}{\partial_x}\left(\sigma_s^{eff}\frac{\partial\phi_s}{\partial x}\right) - j^{Li} - a_{dl}C\frac{\partial(\phi_s - \phi_e)}{\partial x} \qquad \text{Eq.1}$$

with σ_s solid phase conductivity and eff defined as effective parameter. The ϕ_s solid phase potential, ϕ_e liquid phase potential, j^{Li} reaction current of lithium, a_{dl} specific interfacial area, C specific capacitance, and x the distance in the thru-plane direction.

In the same way, the charge conservation for the electrolyte can be expressed as presented in Equation 2:

$$0 = \frac{\partial}{\partial_x}\left(k^{eff}\frac{\partial\phi_e}{\partial x}\right) + \frac{\partial}{\partial_x}\left(k_D^{eff}\frac{\partial lnc_e}{\partial x}\right) + j^{Li} + a_{dl}C\frac{\partial(\phi_s - \phi_e)}{\partial x} \qquad \text{Eq.2}$$

with k^{eff} electrolyte effective ionic conductivity, and c_e the Li⁺ concentration in the electrolyte. The k_D^{eff} is the diffusional conductivity that can be obtained by Equation 3:

$$k_D^{eff} = \frac{2RTk^{eff}}{F}(t_+^0 - 1)\left(1 + \frac{dlnf_\pm}{dlnc_e}\right)$$ Eq.3

with R the gas constant, T temperature, F Faraday's constant, and t_+^0 transference number.

The charge transfer (j^{IC}) in a conventional electrochemical system is defined using the Butler-Volmer equation in the form presented in Equation 4. The equation is derived considering the charge neutrality principle of an electrode-electrolyte interface and governs the net charge production rate by summing the forward rate of current production and the backward rate of current production. This equation can be presented in several forms. A detailed discussion about the equation derivation and its application can be found in [35].

$$j^{IC} = a_s i_0 \left\{ exp\left[\frac{\alpha_a F}{R_u T}\left(\eta - \frac{R_{SEI}}{a_s}j^{Li}\right)\right] - exp\left[\frac{\alpha_c F}{R_u T}\left(\eta - \frac{R_{SEI}}{a_s}j^{Li}\right)\right]\right\}$$ Eq.4

where a_s volume specific reaction surface area, i_0 exchange current density, α charge transfer coefficient, R_u universal gas constant and R_{SEI} resistive film layer. The over potential, η, can be defined as the difference between the solid and liquid phases potentials, minus the open-circuit potential of the solid (Equation 5):

$$\eta = \phi_s - \phi_e - U$$ Eq.5

with U the open-circuit potential of the solid.

Species conservation in the electrolyte and active materials.

In an electrochemical system, the species are also conserved during its operation [36]. Therefore, conservation equations can be devised for both the electrolyte and the active material. In the case of the electrolyte, its conservation can be determined by Equation 6:

$$\frac{\partial}{\partial_x}[\varepsilon c_e] = \frac{\partial}{\partial_x}\left(D_e^{eff}\frac{\partial lc_e}{\partial x}\right) + \frac{1 - t_+^0}{F}j^{Li}$$ Eq.6

with ε porosity. Tortuosity effects (D_e) are accounted in both the electrolyte diffusion coefficient and ionic conductivity by the Bruggeman factor showed in Equation 7 and Equation 8:

$$D_e^{eff} = D_e \varepsilon_e^p$$ Eq.7

$$k^{eff} = k\varepsilon_e^p$$ Eq.8

The species conversation for the active material can be written as presented in Equation 9:

$$\frac{\partial c_s}{\partial_x} = \frac{1}{r^2}\frac{\partial}{\partial_x}\left(D_s r^2 \frac{\partial c_s}{\partial r}\right)$$ Eq.9

with r particle radius, D_s diffusion constant.

Theoretical capacity and stoichiometry for a battery cell.

During the battery operation not all the Li content within the active material can be cycled. In this sense, the theoretical capacity $C_{s,max}$ may not the best parameter to represent the working capacity of the battery cell. Conventionally, the maximum usable capacity of a cell is defined by its first discharge capacity. In addition, other parameters as the ratio between the mass specific first charge capacity (q_{fcc}^{cat}) and mass specific first discharge capacity (q_{fdc}^{cat}) divided by their mass specific theoretical capacity (q_{th}^{cat}) can be used to express how the cell deviates from its maximum capacity as shown in Equation 10 and Equation 11.

$$\gamma_{fcc}^{cat} = \frac{q_{fcc}^{cat}}{q_{th}^{cat}} \qquad \text{Eq.10}$$

$$\gamma_{fdc}^{cat} = \frac{q_{fdc}^{cat}}{q_{th}^{cat}} \qquad \text{Eq.11}$$

with γ is the ratio of first discharge and first charge capacity. Therefore, the cathode stoichiometry can be defined as presented in Equation 12:

$$Stoichimetry = \frac{C_s}{C_{s,max}} \qquad \text{Eq.12}$$

The equations presented above are solved using the commercial code GT-Autolion. Initially, the battery cell was characterized in this software to represent the real behaviour of the cell. This was done by calibrating some of the parameters of the above-mentioned equations.

The open circuit voltage was used to characterize factors such as first charge capacity and first discharge capacity. Data from Batemo® website was used for this calibration step [37]. The experiments are done with a 10-channel battery testing machine. The cell is tested in a constant temperature chamber under natural convection (h $=$ 5 $\frac{W}{m^2 K}$). The accuracy for voltage and current reported is ±0.05% FS for both. A genetic algorithm-based optimization routine was used to calibrate the parameters of the equations, having as objective the minimization of the total error between the numerical and experimental OCV curve.

Figure 2 depicts the comparison between the experimental open circuit voltage curve with the results from the optimized electrochemical model. As it can be seen, the model is able to capture the open circuit voltage curve with high accuracy, which states that the electrochemical model of the cell can properly predict the evolution of the potential difference with respect to the battery capacity for a very small current.
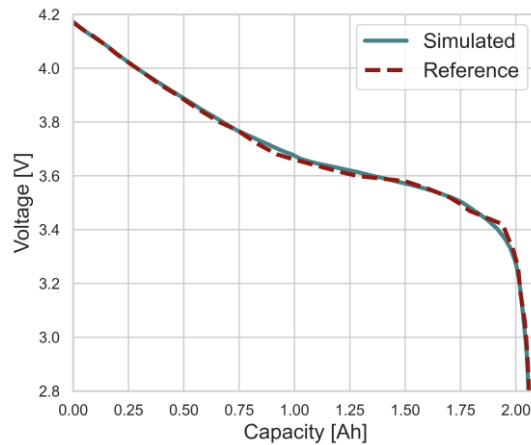
Figure 2- Evolution of the Open Circuit Voltage between experimental [37] and numerical model when discharging at 0.05 Crate and 35°C.

Next, the model validation is extended to different circumstances with boundary conditions representative of those found in real application. In these specific cases, two scenarios were used for the model calibration and verification. A high C_{rate} discharge value (10 C_{rate}) in two different environment temperatures (25°C and 0°C) was selected. Therefore, the instantaneous temperature of the cell is also considering for this case. The energy generated by the cell usage is accounted and compared to those from the experiments by the average cell surface temperature. Figure 3 presents the results of voltage and temperature variation according to the discharged capacity of the battery at 10 C_{rate} and 25°C of environment temperature. As it can be seen, the calibrated model can predict with high accuracy both the voltage and temperature profiles.

Conditions at low temperature and high C_{rate} (Figure 4) do not perform as well as warm conditions (Figure 3). The dependence of the parameters with the temperature variation is a well-known fact. Therefore, the differences can be attributed to small variations on the Arrhenius parameters that are applied in the models to calculate the conductivity of both cathode and anode. Zhang et al. [38] also see similar behaviour and with electrochemical impedance spectroscopy (EIS) and equivalent circuit fitting demonstrate that the primary reason for reduced performance in low temperature lithium-ion cells is an increase in the charge transfer resistance, due to slow reaction kinetics. Nagasubramanian [39] conducted tests on commercial cells adapted to include a lithium reference electrode, concluding that the major contribution to increased impedance at low temperatures was the cathode electrolyte interface. Other studies, such as Ji et al. [40], have demonstrated that reduced Li+ diffusivity in the electrolyte is a significant contributor to reduced performance, particularly at low state of charge. Even in this case, the results allow to conclude that the electrochemical model is robust enough to reproduce the behaviour of the battery cell in terms of temperature and voltage decrease during discharge.

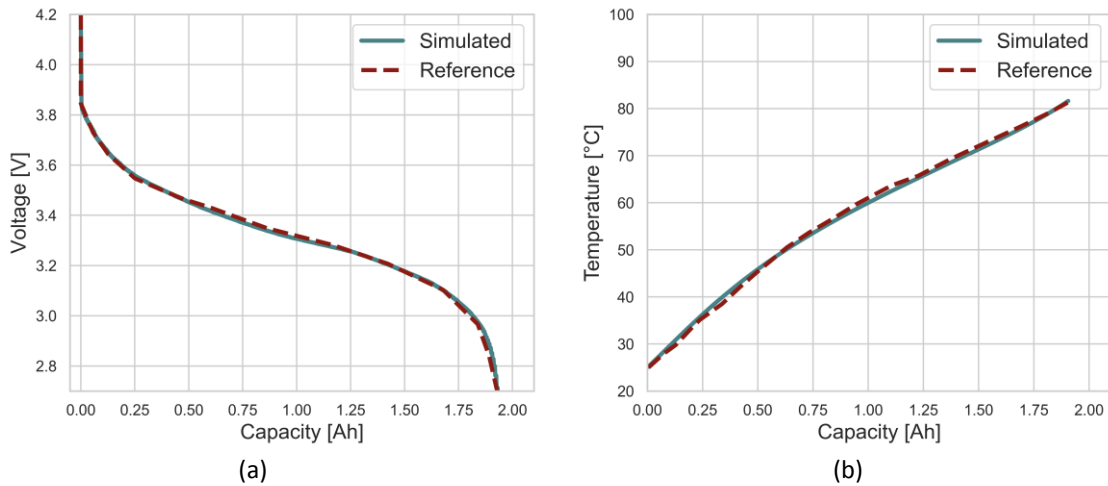(a)   (b)

Figure 3- Evolution of the Terminal cell Voltage (a) and mean temperature cell (b) between experimental [37] and numerical model when discharging at 10 Crate and 25°C.
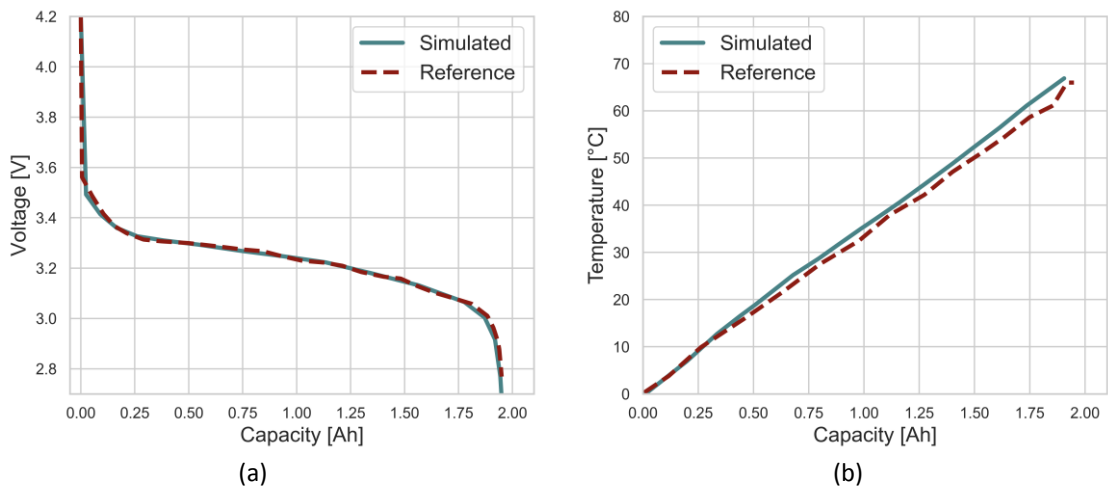

(a)   (b)

Figure 4- Evolution of the Terminal cell Voltage (a) and mean temperature cell (b) between experimental [37] and numerical model when discharging at 10 Crate and 0 °C.

2.2.2. Solid Electrolyte interface formation and lithium plating

As previously stated, the battery cycling can lead to several side reactions that can degrade the battery cell. Among of them, the solid electrolyte interface growing, and lithium plating are known to cause undesirable effects such as capacity loss and increased internal resistance. Therefore, different modelling approaches for these phenomena were pursued along the years. GT-Autolion modelled both electrolyte interface growing and lithium plating with the approach showed in [41] and summarized below:

Solid Electrolyte interface formation

The solid electrolyte interface growth implies a set of steps in which part of the lithium is also consumed in the new layer. This lithium cannot be recovered and decreases the capacity of the cell. This process and the products generated by it are highly dependent on the temperature. Therefore, the correct cell temperature estimation is crucial during the simulation. In this sense, its effects need to be properly accounted in the modelling framework. To do this, first, the diffusion of the solvent (EC) through the solid electrolyte

interface is calculated by means of the Fick's second law (Equation 13), which can provide the material balance in the SEI porous layer:

$$\frac{\partial c_{EC}}{\partial t} = D_{EC}^{eff} \frac{\partial^2 c_{EC}}{\partial r^2}$$

Eq.13

Again, the effective EC diffusivity can account for the tortuosity in the path and for the porosity ε_{SEI} using the Equation 14.

$$D_{EC}^{eff} = D_{EC}(\varepsilon_{SEI})^n$$

Eq.14

The side reaction current density can be also determined considering a Tafel-like kinetic expression as presented in Equation 15.

$$j_{SEI} = -a_s i_{0,SEI} exp\left(-\frac{a_{c,SEI}F}{RT}\left(\phi_s - \phi_e - U_{SEI} - \frac{j^{Li}}{a_s}R_{SEI}\right)\right)$$

Eq.15

The current density can be obtained by dividing the current flux by the volumetric surface area a_s as expressed in Equation 16.

$$i_{SEI} = \frac{j_{SEI}}{a_s}$$

Eq.16

Finally, the variation of the SEI width can be calculated by means of Equation 17, where M_{SEI} and ρ_{SEI} are the molecular weight and the density of the SEI, respectively.

$$\frac{d\delta_{SEI}}{dt} = -\frac{i_{SEI}}{2F}\frac{M_{SEI}}{\rho_{SEI}}$$

Eq.17

The resistance of the SEI layer can be also determined considering the current width of the SEI layer and the effective conductivity of the electrolyte through the porous SEI layer as shown in Equation 18:

$$R_{SEI} = \frac{\delta_{SEI}}{k_{SEI}^{eff}}$$

Eq.18

The effective conductivity of the electrolyte through the porous SEI layer can be also related to the inherent conductivity of the electrolyte via Bruggeman relationship (Equation 19):

$$k_{SEI}^{eff} = k_{SEI}(\varepsilon_{SEI})^n$$

Eq.19

Lithium plating

Lithium plating occurs at conditions where lithium is deposited onto the surface of the graphite particles, decreasing the available surface area of the negative electrode. This behaviour deviates from the normal operation where the lithium is intercalated. This leads to several side effects such as the increase of the SEI layer or to produce dendrites that can originated internal short-circuit in the cell. The Tafel expression (Equation 20) is also used to calculate the current density of the lithium deposition reaction:

$$j_{lpl} = -a_s i_{0,lpl} exp\left(-\frac{a_{c,lpl}F}{RT}\left(\phi_s - \phi_e - U_{SEI} - \frac{j^{Li}}{a_s}R_{SEI}\right)\right) \qquad \text{Eq.20}$$

The variation of the total width of the SEI layer can be determined by Equation 21 summing up the effects from the SEI growth and the lithium plating, being expressed as:

$$\frac{d\varepsilon}{dt} = -a_S \frac{d(\delta_{SEI} + \delta_{lpl})}{dt} \qquad \text{Eq.21}$$

where the variation from the lithium plating (δ_{lpl}) is determined by Equation 22:

$$\frac{d\delta_{lpl}}{dt} = -\frac{i_{lpl}}{2F}\frac{M_{Li}}{\rho_{Li}} \qquad \text{Eq.22}$$

Finally, the variation on the volume specific reaction area can be updated during the calculation to account the decrease of it by both SEI growth and lithium plating. Equation 23 is applied to describe the variation on the volume specific reaction area, where ζ is the morphology factor which indicates the direction at which the side reactions spread in the surface.

$$a_S = a_{S,0}\left[1 - \left(\frac{\varepsilon_0 - \varepsilon}{\varepsilon_0}\right)^\zeta\right] \qquad \text{Eq.23}$$

The application of the set of equations provides a media to quantify the aging of the cell as it is cycled. Both the phenomena (SEI growth and lithium plating) contribute to the capacity loss of the cell. Figure 5 shows the capacity loss is presented for three different environment temperatures, highlighting the dependence of this phenomenon with respect to the boundary conditions of the battery cell. Additionally, the results from Schuster et al. [42] were used to validate the results obtained by the aging model implemented in this work. It is also interesting to see that the increase of the SEI width also impacts the resistance of the battery cell, which may promote enhanced conditions for thermal runaway occurrence. Therefore, the assessment of battery performance near to end-of-life conditions is of utmost importance to guarantee its safety and reliability.

For the aging test, the battery was cycled with 1Crate/-1Crate, respecting the 10% and 90% SOC limits as minimum and maximum capacity of the cell. This type of simulation comprehends not only the capability of calculating the reduction of the cell capacity but also the proper matching of SOC evolution and voltage profile. The case of 35⁰C was used to calibrate the model. The curve of 55⁰C was simulated to validate the proposed constants. Finally, the 15⁰C is simulated to show the temperature influence on the capacity loss. As it can be evidenced, the simulation results match in a great extent those results from experiments allowing to infer that the calibrated electrochemical model is able to represent the real operation of the cell. The cell loosed 3%, 8% and 17% of the initial capacity for 15⁰C, 35⁰C, and 55⁰C. This highlight the importance of maintaining the temperature controlled. In addition, justified the efforts put on developing advanced computational tools for the design of the cooling system. A summary of the calibrated properties for the electrochemical model is presented in Table 2. The values are those

to be used as inputs in the electrochemical model and assures the reproducibility as well as the archival nature of the investigation.
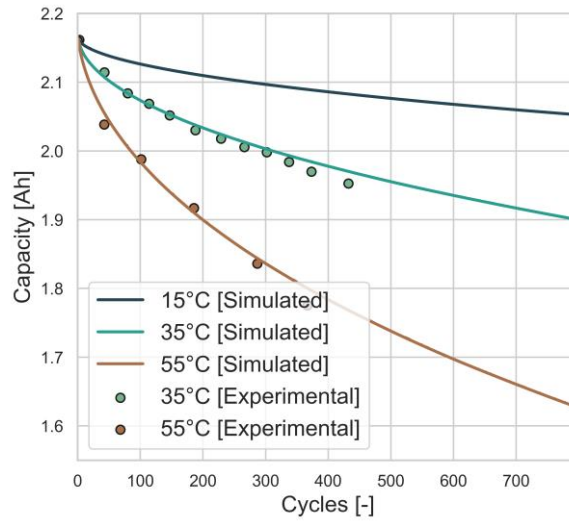

Figure 5- Evolution of the cell capacity at different ambient temperatures (15°C, 35°C and 55°C) when cycling with charge and discharging with 1.0 C_rate.

Table 2 – Final parameters obtained from calibration.

Parameter	Min Optimizer	Max Optimizer	Optimum Value
ε_0 [-]	0.10	0.20	0.15
M_{SEI} [-]	100	160	135
ρ_{SEI} [-]	1.3	2	1.6
Contact resistance [mOhm·m^2]	0.20	0.30	0.26
Initial Film Thickness [nm]	2	10	5
U [V]	3.5	5.0	4.18
q_{fcc}^{cat} [mAh/g]	150	230	190
q_{fdc}^{cat} [mAh/g]	160	220	182
q_{fcc}^{an} [mAh/g]	200	420	372
q_{fdc}^{an} [mAh/g]	200	400	350
N/P [-]	1.0	5.0	1.1
Capacity loading [mAh/cm^2]	2.0	7.0	4.0

2.2.3. Thermal decomposition reactions

Battery thermal abuse has been identified as a critical issue for high density Lithium-Ion batteries. Its occurrence may lead to a set of chain reactions with high energy release known as thermal runaway. Therefore, a set of reactions was also included to describe this phenomenon. These reactions involve the decomposition of the main components of the battery cell as electrolyte, positive and negative electrode, and the solid electrolyte interface. Different authors have investigated the dominant reactions that could affect the thermal runaway attempting to attain Arrhenius based mechanisms to describe the evolution of the phenomena [43][44]. Table 3 presents a summary of the most recent mechanisms for the thermal runaway prediction. The table is divided in anode and cathode materials, as well as the electrolyte, binder and geometry studied. The mechanisms devised by Hatchard et al. [45], Kim et al. [46] and Bilyaz et al. [44] proposed a description of the decomposition for LiCoO$_2$ cathode (LCO) chemistry. Since

this work deals with a modern cathode chemistry (NMC 622), the thermal runaway mechanism for this specific chemistry was selected from those available in the literature. As it can be seen, the mechanisms proposed by Kriston et al. [47], Ren et al. [12] and Feng [48] allow to model thermal runaway for NMC cathode and graphite anode which are the same composition of the Samsung 20R battery cell. All the mechanisms proposed in Table 3 were implemented in a Python plug-in called TRKIN, presented by the authors in a previous work [49]. In this work, both Ren [12] and Kriston [47] mechanisms were selected to describe the thermal runaway evolution for NMC chemistry given their superior performance as demonstrated in previous works [49].

Table 3 - Number of reactions considered in the description of the thermal runaway process for each mechanism used in the investigation.

	Anode	Cathode	Electrolyte	Binder	Geometry
Hatchard et al. [45]	Gr	$LiCoO_2$		-	Cylindrical
Kim et al. [46]	Gr	$LiCoO_2$		-	Cylindrical
Bilyaz et al. [44]	Gr	$LiCoO_2$	EMC:EC:DMC	CMC	Pouch
Kriston et al. [47]	Gr	NMC	EC:DMC	CMC	-
Ren et al. [12]	Gr	NMC	EMC:EC:DMC	-	Pouch
Feng et al. [48]	Gr	NMC	EMC:EC:DMC	-	Pouch

The general formulation to determine the reaction rates for each one of the decomposition reactions of the aforementioned mechanism is provided in Equation 24. This general equation can be used independently on the mechanism.

$$R_x = A_x \cdot (c_x)^{n_1} \cdot (1 - c_x)^{n_2} \cdot e^{\frac{E_{a,x}}{R_0 \cdot T}} \cdot g_x \qquad \text{Eq.24}$$

where, $R_0 = 8.3145 \frac{J}{K \cdot mol}$, x the component, $E_{a,x}$ the activation energy, c_x is concentration, n_1 and n_2 dependence exponent, g_x is linear dependence factor and A_x is the pre-exponential factor. The heat released by each one of the decomposition reactions can be obtained by multiplying the reaction rate obtained from Equation 24 by the heating value of each component (H_x) and the total mass of component (m_x), as presented in Equation 25.

$$Q_{TR_x} = m_x \cdot R_x \cdot H_x \qquad \text{Eq.25}$$

Each of the parameters from Equation 24 can be replaced by the values presented in the Table 4 and Table 5 for Kriston [47] and Ren [12] mechanism, respectively. Using the inputs provided in the tables, it can be possible to simulate the decomposition reactions due to the thermal runaway for each of the mechanisms. From the analysis of the tables, it can be argued that the mechanism proposed by Kriston [47] suggests different equations to account not only for the SEI degradation at intermediate temperatures but also for its regeneration as the temperature increases. Additionally, cathode and anode reactions are modelled by two and three reactions, respectively. This allows to have further discretization on the heat release curves during the thermal runaway, as presented in previous findings [49].

Table 4 - Summary of kinetics parameters for each one of the components considered for Kriston et al. mechanism [47].

Reaction	x	A_x	$E_{a,x}$	n_1	n_2	H_x	g_x
-	-	[1/s]	[kJ/mol]	-	-	[J/g]	-
SEI decomp	An	$1.67 \cdot 10^{15}$	1348.96	1	0	1312	$e^{-t_{sei}/t_{sei,0}}$
An+Ele	An	$1.78 \cdot 10^{14}$	1619.96	1	0	479.397	1
An+Bin decomp	Bin	$5.62 \cdot 10^{6}$	963.55	1	0	208.15	1
Cat1 decomp	Cat1	$3.22 \cdot 10^{10}$	1415.21	1	0	100.02	1
Cat+Bin decomp	Cat2	$3.78 \cdot 10^{12}$	2053.56	1	0	212.9	1
Cat3 decomp	Cat3	$1.3 \cdot 10^{6}$	2890.64	1	0	189.02	1
Ele evap	Ele	$2.23 \cdot 10^{7}$	951.50	1	0	-62.5	1
Ele decomp	Ele	$5.14 \cdot 10^{25}$	22763.79	1	0	155	1
Ele oxidation	Ele, O_2	$5.14 \cdot 10^{18}$	1264.66	1	0	2000	$[c_{O_2}]^{n_1}$

Table 5 - Summary of kinetics parameters for each one of the components considered for Ren et al. [12] mechanism.

Reaction	x	A_x	$E_{a,x}$	n_1	n_2	H_x	g_x
-	-	[1/s]	[kJ/mol]	-	-	[J/g]	-
SEI decomp	Sei	$6.3623 \cdot 10^9$	109.6	5.5	0	578.7	1
An+Ele	An	$5.151 \cdot 10^{17}$	200.77	1	0	253.2	1
An+Bin decomp	BinAn	$4.9679 \cdot 10^{15}$	195.49	1	0	108.5	1
Cat decomp	Cat	$5.3481 \cdot 10^5$	109.34	1.5	0	434	1
Cat+Bin decomp	BinCat	$6.5429 \cdot 10^{13}$	177.85	2	0	452.1	1
Cat+An	An	$2.4262 \cdot 10^{13}$	162.01	1	0	560.6	1
Ele evap	Ele	$2.23 \cdot 10^7$	951.50	1	0	-150	1

Table 6 and Table 7 represents the initial concentrations for each one of the compounds and the closure for the reactions that may occur with similar species. It is evident that the anode can be decomposed not only by its reaction with the electrolyte but also by reacting with the binder. In this sense, mass coupling equations are needed. For example, to track the decomposition of the anode, for each time step, the variation of its mass fraction will be a consequence of the variations calculated for the anode decomposition reaction from its reaction with the electrolyte and with the binder. The same relations can be derived for each one of the remaining components. It is worth to mention that the Ren mechanism [12] here presented includes a modification to account also for the electrolyte evaporation at the early stages of the thermal runaway.

This effect is evident on several research and may tailor the start of the BTR. Therefore, it must be considered to a proper modelling of the phenomenon.

Table 6 - Initial concentrations and reaction rates for each component used in Kriston mechanism [47].

Component	Initial concentration C_0	dc/dt
Anode	1	-Ran,ele-Rsei
Cathode	1	(-Rcat1-Rcat2-Rcat3)/3
Electrolyte	1	-Re,ev-Re,ox-Re,dec
SEI	1	-Rsei
tSEI	0.033	Rsei
Binder	1	-Ran,b
Cat1	1	-Rcat1
Cat2	1	-Rcat2
Cat3	1	-Rcat3
O_2	0	Rcat2*K_{O_2}-Rele,ox

Table 7 - Initial concentrations and reaction rates for each component used in Ren mechanism [12].

Component	Initial concentration C_0	dc/dt
Anode	1	-Ran-Rcatan
Cathode	1	-Rcat
Electrlyte	1	-Re,ev
SEI	1	-Rsei
t_{SEI}	-	-
Binder	1	-(γ/(γ+1))*RbinAn-(1/(γ+1))RbinCat
BinAn	1	-RbinAn
BinCat	1	-RbinCat

where $K_{O_2} = 0.114472$ and γ=0.56.

Validation of the Thermal Runaway model

The thermal runaway modelling and comparison considering some of the most recent reaction mechanism was recently introduced in the literature by the authors [49]. The referred source addresses both the validation and the comparison of the particularities of each mechanism. For brevity of the manuscript, the validation of the mechanism is here only briefly described showing the results considering the experiments that were presented by the authors of each mechanism. First, the mechanism proposed by Ren et al. [12] is validated in accelerated rate calorimetry tests, with the results presented in Figure 6.
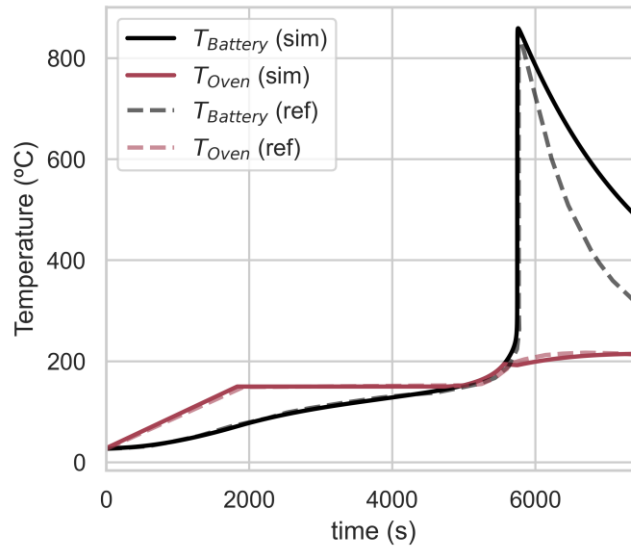
Figure 6 –Comparison between simulated and experimental results considering accelerated rate calorimeter temperatures for both the battery cell and ARC under heating ramp of 150°C.

As it can be seen, there is an excellent agreement between the condition implemented in the current work with that from the original paper in which regards the surface temperature evolution up to the maximum temperature value in the experiment. From this point, discrepancies appear. This is suggested to be a consequence of differences in the convective heat transfer coefficient that is reported in the original work with the one that was used in the experiments. This claim is supported by the fact that the cooling phase has an analytical solution, since it consists only of the Newton cooling law. The formulation of the problem is simple and should lead to a closed solution. Results reported by Zhang et al. [50] also demonstrates such discrepancies, indicating a similar reason for them.

In a second step, the Kriston et al. [47] mechanism was also validated considering the differential scanning calorimeter tests provided in the original work for the Anode and Cathode components. The results of the validation are presented in Figure 7. As it is shown, the results obtained by the simulation code matches those from the experiments in the complete temperature spectra, which confirms the validity of the implemented mechanism for the paper.
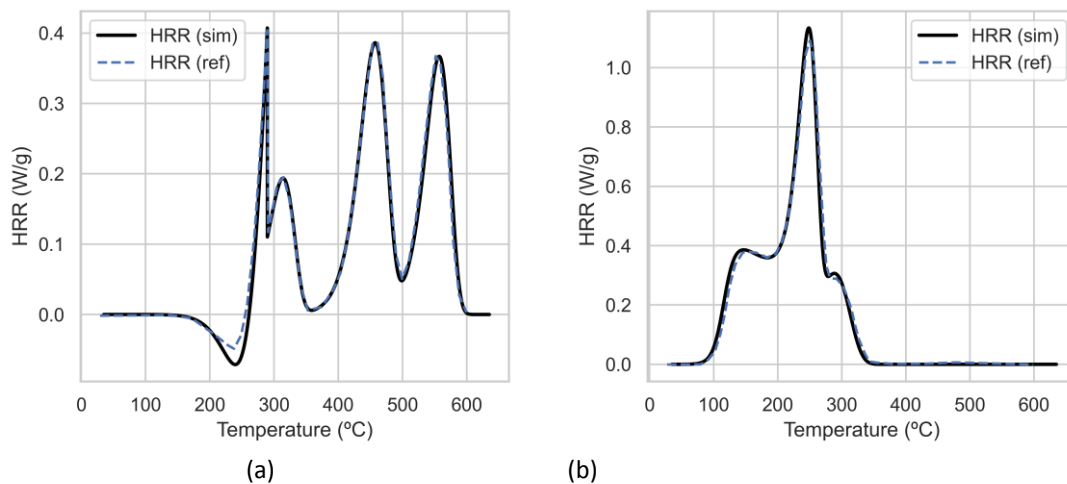
Figure 7 – Comparison of anode (a) and cathode (b) heat release profiles from experiments and simulation. The experimental results are obtained from scanning calorimeters of [47].

Therefore, it can be concluded that the reaction mechanisms for thermal degradation implemented in this work can reproduce the degradation of components due to thermal abuse and associated heat release showed in dedicated works for the evaluation of BTR in NMC cells. It is important to remark that the instantaneous temperatures reported in the manuscript are those for the interior of the cell and not those from the surface, which are generally reported in the literature. It is believed that the use of the internal temperature adds archival nature value, since it can allow to understand the heat transfer mechanisms inside of the cell, instead of neglecting them.

2.3. Cooling System

Thermal issues associated to BEVs and HEVs battery packs can significantly affect the performance and life of the battery. To keep the battery operating at the ideal parameter ranges, the discrepancy between the optimum and operating conditions of the batteries needs to be reduced significantly by implementing thermal management systems. These systems are utilized to improve the battery efficiency, by keeping the battery temperature within desired ranges [51]. Generally, the overall vehicle TMS is composed of the radiator coolant loop for the ICE (case of HEV) or electric machine (case of BEV), power electronics coolant loop, drive unit coolant loop, air-conditioning (A/C) loop and battery coolant loop [52]. Even though all the circuits mentioned above have significant roles in enabling the vehicle to operate as robustly, efficiently, and safely as possible, in BEVs and HEVs, most of the focus is given to battery pack circuit due to its direct effect. It is important to notice that some of the abovementioned coolant loops are communicate, others are independent due to the different working temperature ranges, e.g. ICE (≈90°C) and battery (≈30°C).

Batteries generally work efficiently over a narrow range of discharge rates and operating temperatures. In addition, the uniformity is crucial for each battery cell [53]. Indirect liquid refrigerant cooling is a compact way of cooling the battery, with more flexibility compared to air cooling with the fan and ducts. Heat generated by the battery is transferred to the refrigerant that circulate in pipes around the batteries. The liquid used is usually 50/50 mass percentage water-glycol mixture and it is kept cool via a heat exchanger with air as an ICE cooling loop or a heat exchanger connected with the A/C

system [17]. For this work, a complete indirect liquid cooling is designed and modelled based on a well-known commercial cooling systems used by Tesla for cylindrical cells [54]. As the main objective is to show a novel methodology for evaluating a real battery package, the cooling system is like a commercial application. The methodology for the modelling is based in the following steps: 1) Create the cooling system and battery cells in Computer-Aided Design (CAD) with details in terms of materials and real size (SOLIDWORKS 2020®) (Figure 8a and Figure 8b), 2) Load the CAD in GEM3D® (tool that allows to pass 3D models of flow, thermal, and mechanical systems into model files for using them with GT-SUITE®), define the thermal connection between components and set the element discretization to create the mesh for Finite Element Method (FEM) solution. 3) Create the GT Suite model and add the battery electric model (Figure 8c). Lastly, 4) Run the simulation case with different cooling setups and electric loads. Since experimental temperature values were not available to perform a model validation of the battery model, the authors have guided their meshing setup with previous works. In [4], the authors have assessed the temperature distribution of piston, cylinder head and cylinder walls by means of the same FEM approach herein presented and have validated the results with spatial distribution temperature experiments. Giving the similarity of the problem (flow-wall interaction), the authors have followed the same approach. A mesh independence was evaluated and presented in Appendix B.

The complete cooling system (pipes outside of the battery module, pumps, and heat exchangers) will not be modelled in this manuscript. This relies on the fact that the main objective of the work is to understand the interplay between the local thermal conditions in the battery cell, which are dependent on the heat transfer between the battery cells with the cooling plates. Therefore, the temperature and flow will be fixed for each simulation. The temperature of the coolant (50/50 mass percentage water-glycol mixture) is fixed in 30°C as well as the ambient temperature during the simulation. The battery electric load can be set in terms of required power, voltage or current. In this case, current rate was set to simulate extreme charging conditions critical for thermal runaway. Operating conditions regarding coolant flow, C_{rate} and environment temperatures were obtained from the literature [23][21].

(a)   (b)
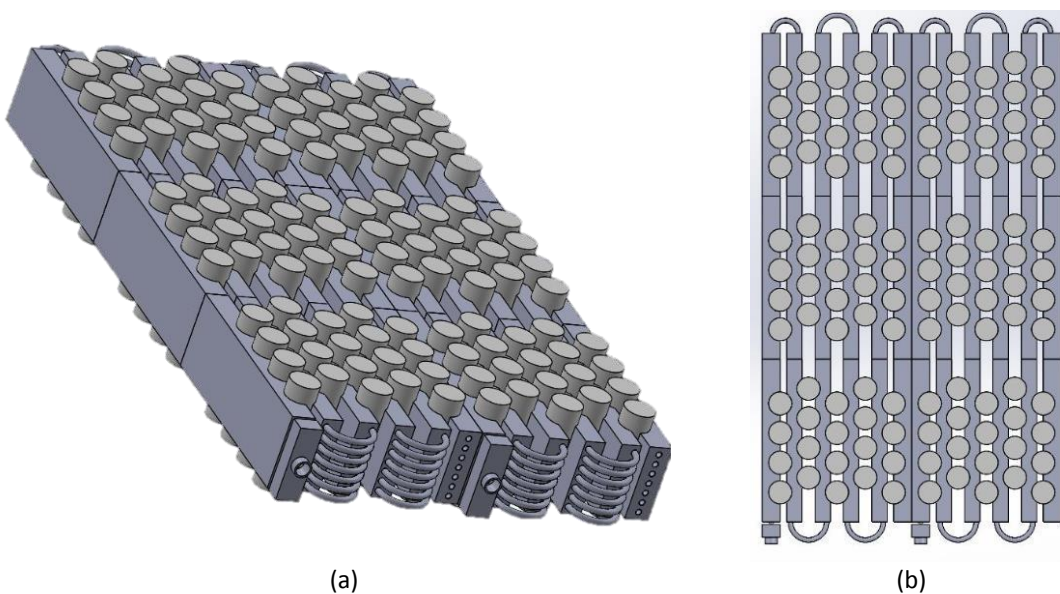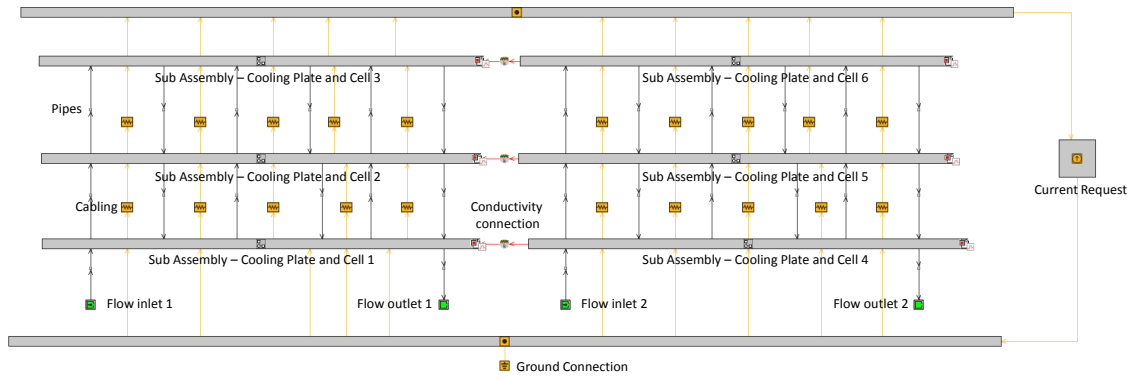
(c)

Figure 8 – Battery cooling system for cylindrical 18650 Samsung 20R cells. Design of the battery module with 120 cylindrical cells isometric (a) and top (b) view and the scheme of GT-Suite battery system with flow and electrical connections (c).

As seen in Figure 8, the cooling system is an indirect cooling plate arrangement. Each plate touch 4 cells. Three series and twelve series plates were designed to control the temperature of the 120 cells. In Figure 8 is possible to see a space between parallel plate to be able to connect the pipes at the end of the arrangement of 3 consecutive plates. This means that each cell in opposite location have a surface with air contact (natural convection). The rest of the lateral surface is in contact with the cell. In addition, only 80% of the cell, in vertical axis, is in contact with the plate. The top and bottom is under natural convection with the ambient too. This is done to show the flexibility of the methodology proposed to simulate complex set ups. Seven tubes per plate were designed with 3 mm diameter to cold down the plate homogeneously. The pipe collector was designed with a volume of 2.3 cm^3.

2.4. Coupling methodology and solution framework of the sub models

The three parts previously described (electrochemical, thermal decomposition and cooling description) were coupled together in GT-Suite environment. Figure 9a represents the three parts that were coupled and the information that flows from one part to feed the next routine. Temperature field calculation is solved in a fully coupled manner. This means that the heat from the different sources is accounted in the energy conservation equation as presented in Equation 26.

$$\rho C_p \frac{\partial T}{\partial t} = \lambda \nabla^2 T + \ Q_{TR_x} + Q_{gen} \qquad \text{Eq.26}$$

$$Q_{gen} = I(E_o - E + T\frac{dE_o}{dt}) \qquad \text{Eq.27}$$

The heat generated is modelled with Bernardi model [55] presented in equation 27. The I is the battery current; E_o is the battery open circuit voltage, E is the cell voltage, T is the battery temperature, $\frac{dE_o}{dt}$ is the temperature coefficient. This heat comes from irreversible heat sources attributed to three different contributions. First, heat sources due to main reactions at the solid/electrolyte interface, which also consider

contributions due to SEI growth and Li plating currents. Second, ohmic losses in the electrolyte because of electron and ion transport within the cell and third, irreversible heat source originating from Li transport inside secondary active particles. Lastly, reversible contributions are attributed to the reaction entropy change during intercalation at the cathode and anode. For more information, please refer to the work of Jiaqiang et al. [20]. The cell is considered as a thermal mass with anisotropic material properties. The thermal conductivity was taken from [56] with 0.8 W/mK in radius-axis, 27 W/mK in vertical-axis and 0 W/m K in Θ-axis. The specific heat (C_p) of the cell is 860 J/kg K and density (ρ) is set as 2660 kg/m^3. This is important for the prediction of the gradient across the body of the cells. The cooling plates are modelled with properties of aluminium by a thermal mass with FEM approach as the battery cells. As it can be seen, the heat generation from thermal runaway is considered as a heat source inside of the energy conservation equation. In the same way, both the electrochemical and aging model are solved together. This indicates that the specie conservation equations accounts terms of generation or consumption from the different mechanisms that takes place during the battery operation. It should be remarked that the variation of species concentrations from thermal degradation is still not coupled to the remaining species conservation equations. Considering the SEI for instance, the interplay that could exist between the SEI growth from the electrochemical model and the SEI decomposition from the thermal runaway are not considered in a coupled manner. It is believed that a further refinement of the model could be attained if the equations are coupled. Nonetheless, the nature of the thermal runaway phenomena dominates the species evolution once it starts to occur, which may decrease the significant of having the coupling of species conservation reactions.

Regarding the solution framework, Figure 9 shows a scheme of the approach used in this work. The simulation starts by setting an initial temperature for the battery cell. This temperature is used as input for the thermal runaway code, which calculates, considering the initial concentration, if this temperature results in decomposition of the components and the energy release associated with the process. This energy released is summed to the energy output from the irreversible losses calculated by the electrochemical model. Next, the total heat is inserted in the cooling system, where the heat equation is solved, and the new temperature of the battery cell is determined. This loop is solved for each time step, allowing to monitor the different phenomena and investigate the critical operating conditions that may leads to battery fail. Additionally, since all the battery cells can include the thermal runaway description, this methodology allows to understand the impact of a single battery failure in the system and the heat spread along the battery module, pack, and cooling system. To speed up the process a conversion from the electrochemical cell model to an equivalent electric circuit (RC branches) was performed. For brevity of the manuscript a detailed description of the model, conversion routine and the validation are presented Appendix A. A summary of the simulation approach is presented in Figure 9a.

To induce the BTR of one of the cells and study the temperature distribution in all the battery module, a cell in the middle of the module (cell 8.6 in Figure 9b) was triggered. in this model, this means to add an experimental heat release profile measured in a high temperature continuous flow vessel by the authors in a previous work [57]. At the same time, the battery module was submitted under C$_{rates}$ of 5 and 10, representing fast

charge and high discharge demand of state-of-the art systems [58][59]. Figure 9b presents the case of study developed to demonstrate the methodology developed for description of the interplay between the different phenomena.

(a)
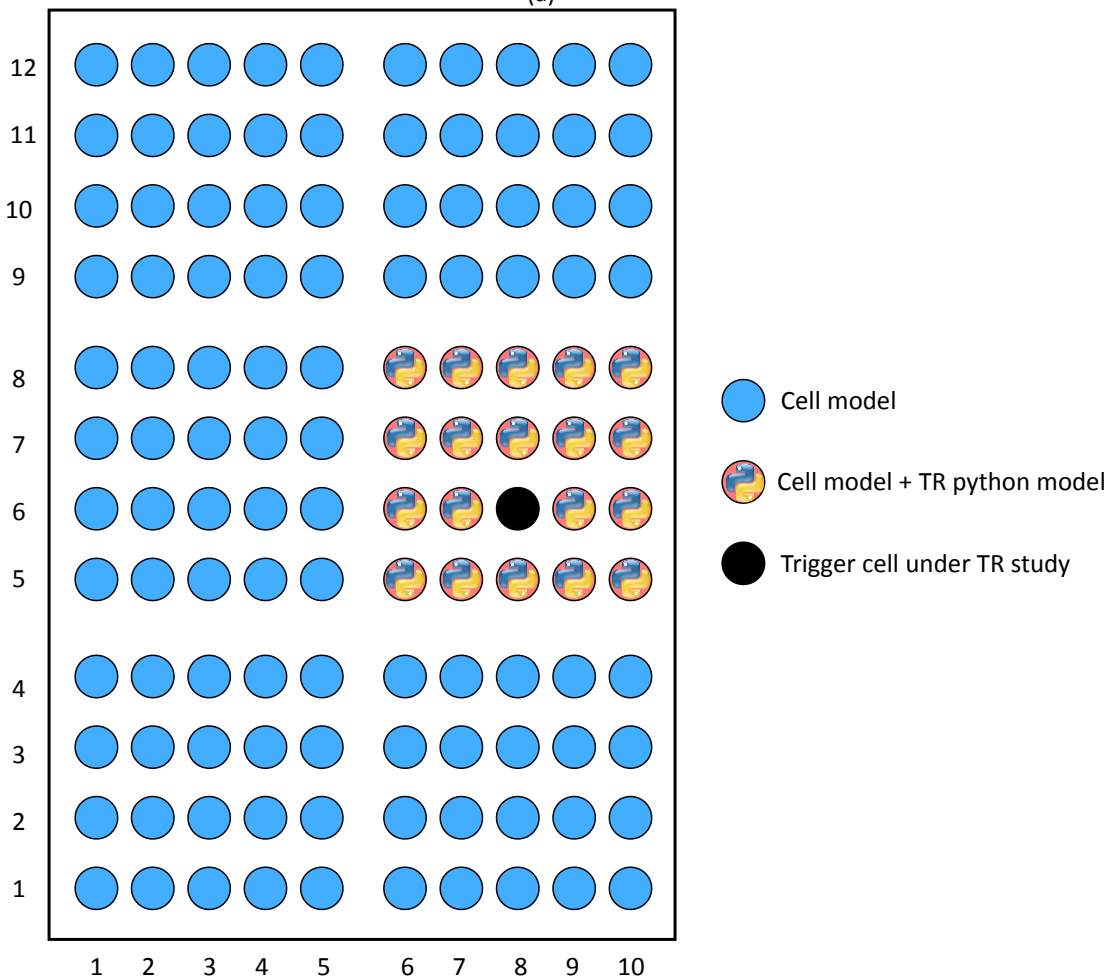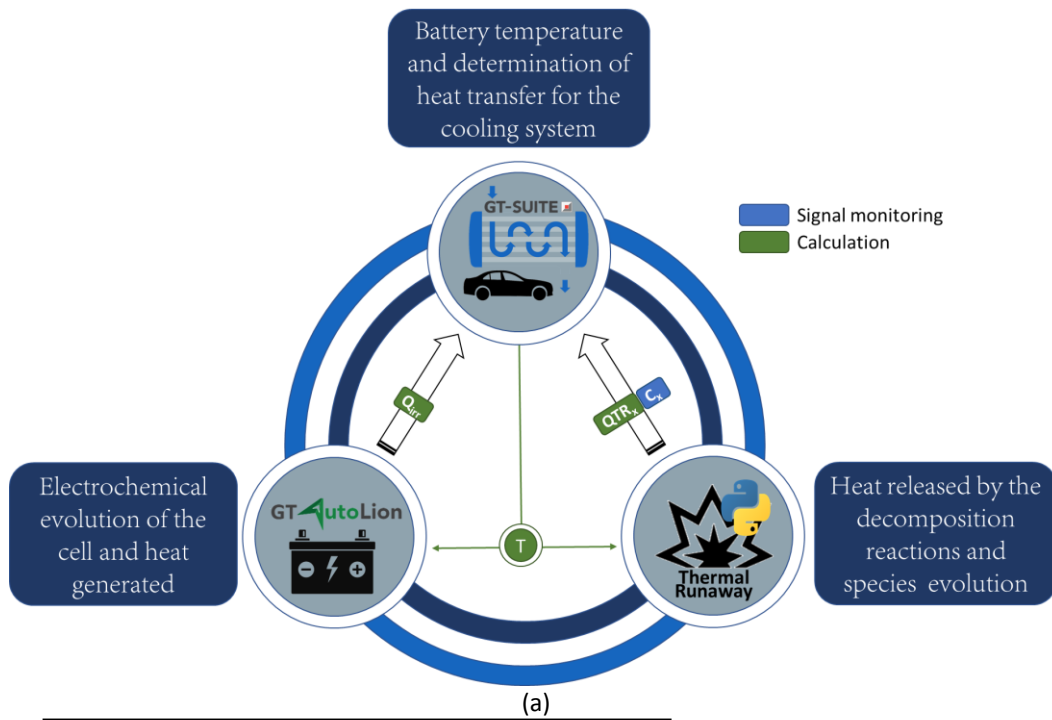
(b)

Figure 9 – Scheme of the methodology proposed to study Lithium-Ion cells under normal and thermal runaway conditions (a) and the battery cooling layout with the TRKIN coupling in the middle-right side of the battery pack (b).

3. Results and discussion

The results section is divided into two different parts. First, the effect of different coolant flow mass and current solicitation (C_{rate}) is studied with a variation of 3 flow rates (3 g/s, 20 g/s and 50 g/s) in each entry (the module of 120 cells have two entry and two out pipes) and two discharge C_{rate}: 5 and 10. In a second subsection, the cell aging on the heat transfer phenomenon is assessed by considering the temperature distribution in the pack as well as the different heat transfer mechanisms that are present in the cell. Lastly, thermal runaway modelling is coupled to 20 different cells inside of the pack to identify the evolution of the pack failure with time. Two different mechanisms are used to identify the effect of the different decomposition modelling on the thermal runaway evolution.

3.1. Flow and C_{rate} effect in battery temperature

The battery module (120 cells) arranged in 10 parallel cells (20 Ah) and 12 series cells (43.2 V) are tested in continuous C_{rate} (5 and 10) from state of charge (SOC) 1.0 (fully charged) to 0.2 (cell depleted up to the safety point). This takes 576 s and 288 s for 5 C_{rate} and 10 C_{rate}, respectively. The simulation as provides complete temperature distribution, flow pressure drops and heat transfer solution, takes 20 times the real time. Despite being slow compared to a simple battery pack without cooling resolution, the solution proposed can be coupled with a complete powertrain model. The time to perform a simulation of a homologation driving cycle as WLTC (30 minutes) can take 10 hours in a normal desktop computer.

Figure 10 shows the average cell temperature at the end of the simulation (576 s and 288 s for 5 C_{rate} and 10 C_{rate}) when the battery SOC arrives to 0.2 for the complete module. The 120-cell average temperature are depicted in colour bar ranging from 30°C to 80°C. For 3 g/s in each entry, the central cells achieve the maximum acceptable temperature at 5 C_{rate} and overpass for 10 C_{rates}. For this last case is dangerous for the battery performance because is close to temperatures where the SEI can be decomposed. Ren et al [12]shows that the SEI start to react and generate heat at 110 °C.

When increasing the flow rate, the cells reduce the average temperature from 47°C with 3 g/s to 39°C with 20 g/s and 38°C with 50 g/s (average of the 120 cells) at 5 C_{rate}. The other C_{rate} is an extreme case for the cells because is in the recommendable limit by the manufacturer. The cooling has a good performance only above 20 g/s with an average temperature of 59°C. For 3 g/s the average temperature is 73°C with maximum local average of 82°C. Moreover, the simulation results show that the model is sensible for temperature distribution depending on the position of the cells with respect to the entry of the coolant, the surrounded cells and cooling plates. Despite column 1 and 6 of cells

being in the entry of the coolant flow (fixed at 30°C), the results are not the same due to the contact of column 6 of cells with column 5 at the left side and column 1 contact with air at the left. The same can be seen between column 5 and column 10 but in the right side of the cell.
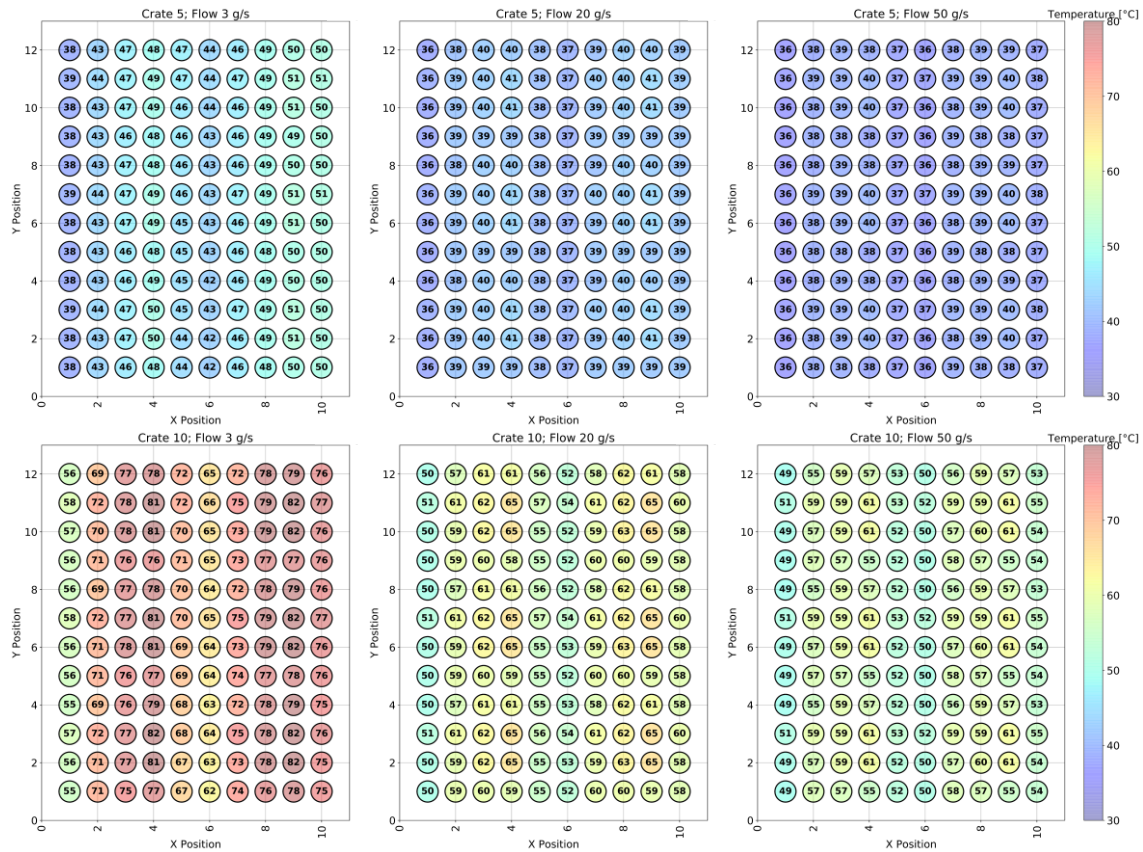

Figure 10 – Average temperature of the cells at different C_{rates} and coolant flow rates in the last simulation instant (SOC = 20%).

The model is capable to describe the 3D temperature distribution by the finite element method. As the surface was divided and connected with different parts of the cooling system (conduction with plates and convection with air), an accuracy temperature distribution is obtained.

Figure 11 shows the temperature distribution for the cell 1-1 (most cold cell due to being in the entry and contact with air in the left side) and cell 8-6 (hot cell because is in the middle right side of the pack) characteristic cells of the module (see Figure 10). The cell 1-1 (Figure 11a) with an average temperature of 38°C, 36°C and 36°C, with the variation of the flow rate for 5 C_{rates} has a central cold part in the left zone due to the absence of other cell in the module in contact with the cooling plate. Also, the central part is in contact with the cooling plate while the top and bottom with the air. For 3 g/s, the temperature variation is higher than 10°C. However, when the flow is increased the variation is reduced below ±2.5°C (acceptable following fabricant recommendations). As cylindrical cells have high thermal conductivity along the length and low conductivity in the radial direction, the temperature distribution is more homogeneity in the vertical

plane than in the radial plane. This is possible to see in both C_{rates} tested. However, as more energy is generated for 10 C_{rates}, the temperature difference is higher.

For 10 C_{rates}, the cooling system have more difficulties to achieve a homogeneous temperature with average of 55°C, 50°C and 49°C and variation in the cell of ±12.4°C, ±9.1°C and ±8.8°C. This is mainly due to the asymmetric of the cooling system. The cell 8-6 (middle right of the module) has a temperature variation for 5 C_{rates} of: ±4.2°C, ±5.0°C, ±5.1°C and for 10 Crates of ±12.5°C, ±15.5°C and ±15.8°C. The average temperature is higher than the cell 1-1 because of the surrounding cells and the higher temperature of the cooling system in that zone.
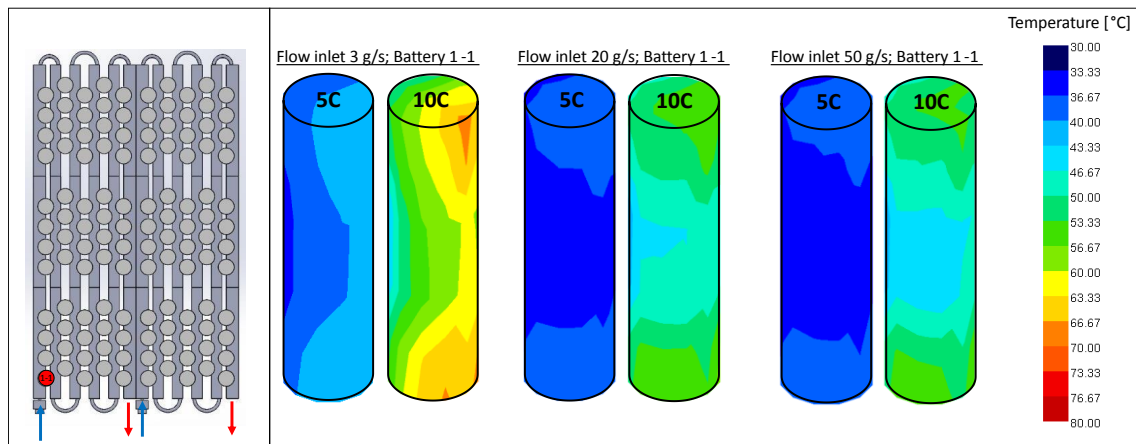
(a)
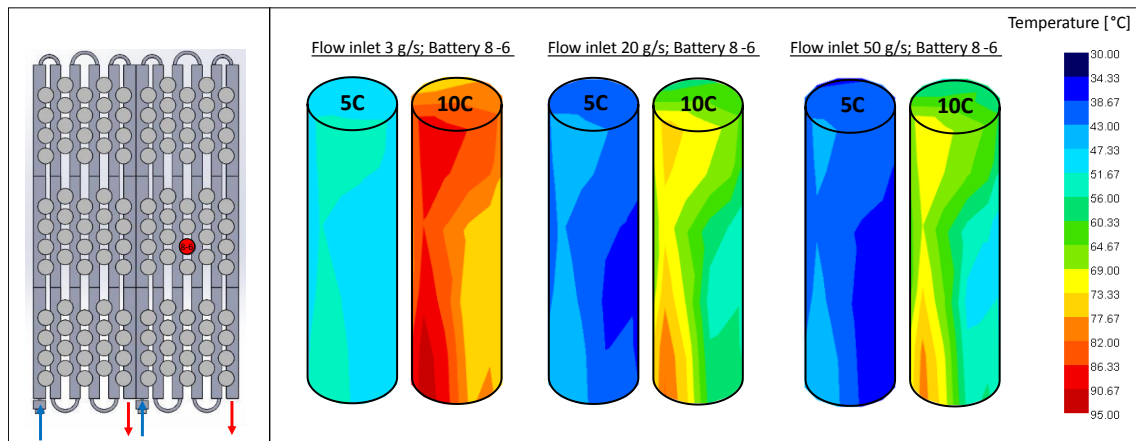
(b)

Figure 11 – Battery cell temperature distribution for cell 1-1 (a) and cell 8-6 (b) in the last simulation instant (SOC = 20%) for the case of 5 C_{rate} (left cell) and 10 C_{rate} (right cell) with different inlet coolant mass flow (3, 20 and 50 g/s).

Figure 12 shows the heat exchange and temperature behavior of the cell along the time for the same cells presented in Figure 11. The main cooling method for the cell is the conduction with the cooling plates. The convection with the ambient is negligible. The heat source (joule losses by the cell named as electric heat) have low variation. The difference that can exist is due to the difference of the cell temperature and the internal resistance change with that parameter. Also, the internal heat is depicted in Figure 12a

and Figure 12b for 3 g/s and 50 g/s, respectively, at 5 C_{rate}. As it can be seen, the highest the temperature differences, higher are the differences in the internal heat. A final remark needs to be done regarding the cooling rate effect on the temperature variations and the consequent heat generation. It is evident that higher cooling flows allows for a capped increase in temperature, which results in very small differences in the heat generated in cell 1-1 and cell 8-6.
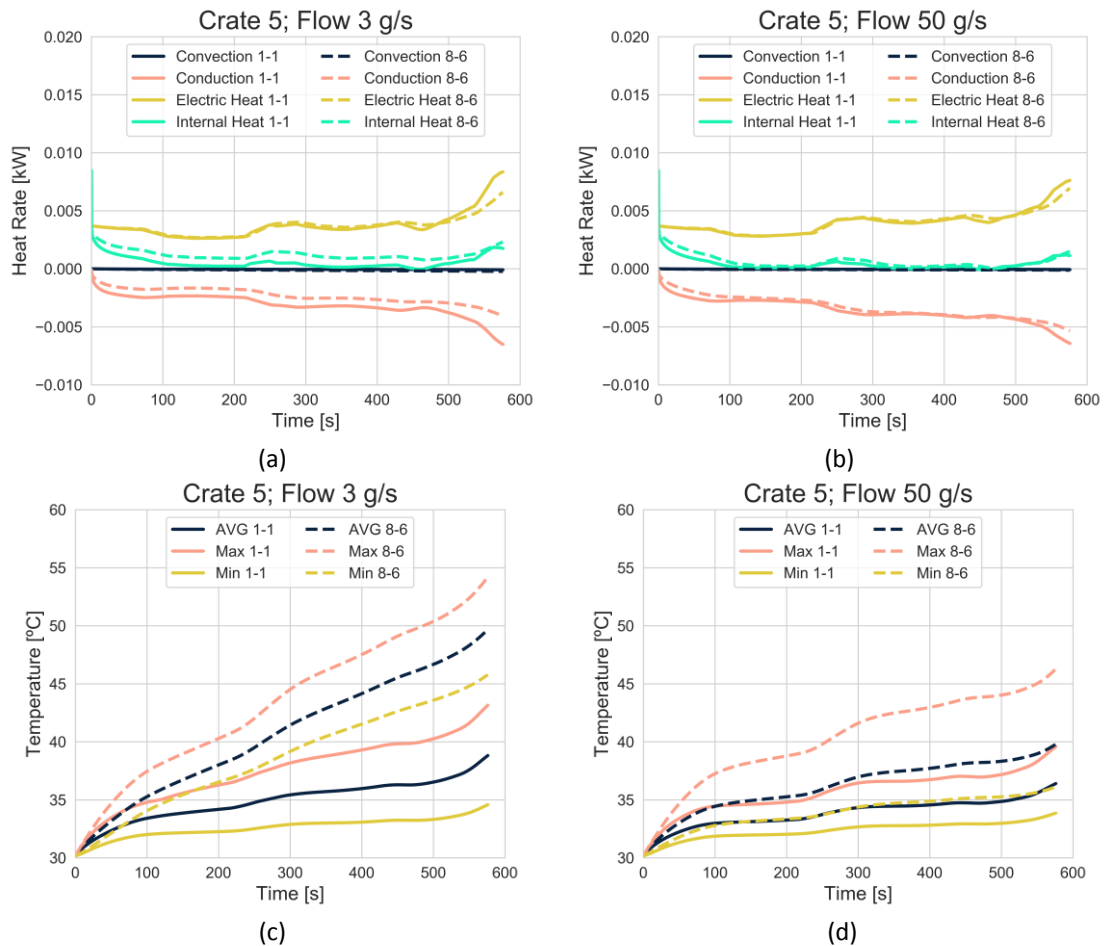

| | (a) | | (b) |

| | (c) | | (d) |

Figure 12 – Heat rate for cell 1-1 and 8-6 when 5 Crate discharge is requested and the cooling flow is 3 g/s (a) and 50 g/s (b). The Average, Maximum and Minimum temperature for 3 g/s (c) and 50 g/s (d) is also presented.

3.2. Aging effect in battery temperature

A comparison between fresh and aged cells was performed using the GT-AutoLion to build an aged cell with 500 cycles. The results are later used to calibrate an equivalent circuit model (see Appendix). The total capacity decreases from 2.1 Ah to 1.8 Ah and the internal resistance increases. Therefore, higher cell losses are expected. For the brevity of the manuscript, only the case of 5 C_{rate} and two flow rates (3 g/s and 50 g/s) is shown in Figure 13. Also, shows the final average temperature of the cells in the last instant of discharge and the differences with the results showed for the fresh cell. For the lowest flow rate, the difference is in average for the 120 cells of 4.2°C. The aged cells closer to the coolant entry showed less difference with the fresh cell due to higher cooler capacity. The same behavior is seen when increasing the coolant rate. The difference

between the aged and fresh cells for 50 g/s are lower than for the case of 3 g/s due to better performance of the cooling system (average difference was 2.5°C).
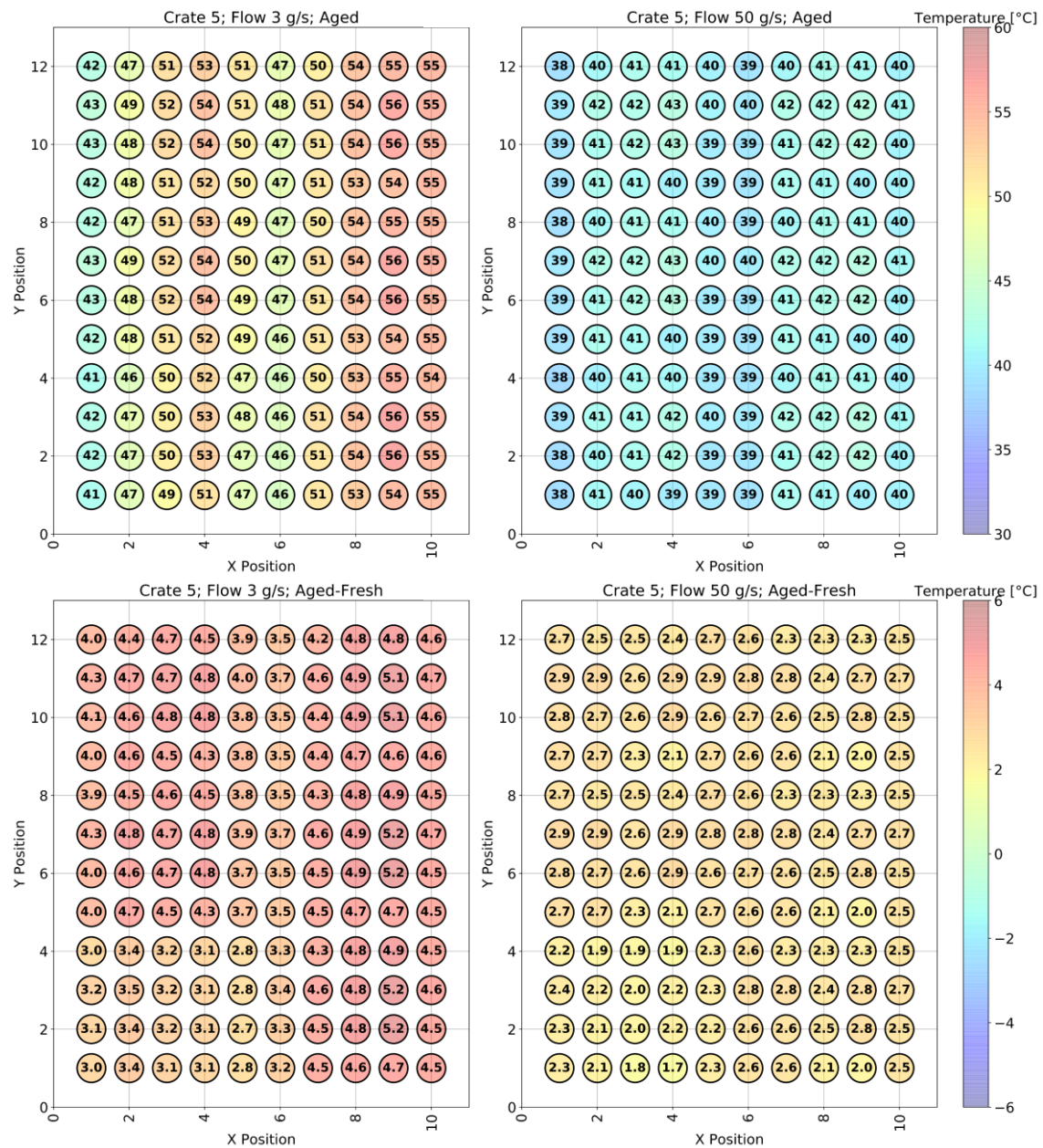

Figure 13 – Average temperature of the cells at 5 C_{rates} discharge and two coolant flow rates (3 g/s and 50 g/s) in the last simulation instant (SOC = 20%) for a 500 cycles aged cell and the difference with the fresh cell.

To understand in depth the causes of the differences found between aged and fresh cells, the energy balance, and temperatures of the cell 8-6 along the time are showed in Figure 14. The higher differences are seen for the lowest cooling flow rate (Figure 14c). In addition, it is possible to observe that the temperatures difference increases in the last phase of the experiment. As the battery is discharging, this means that it is operating in the low SOC range. It is possible to see in the calibration results of both cells that the aged cell has higher internal resistance difference with respect to the fresh in the range 0.4 to 0.1 SOC. Therefore, the cell at low state of charge starts to increase the joule

losses (Figure 14a). This has a direct effect in the increase of the cell temperature after 400 s. For the case of 50 g/s, the conduction increases reducing the gap between the fresh and aged cases. The same results can be seen for the other 119 cells. However, for the brevity of the manuscript these results are not showed. The methodology proposed shows the capability of studying fresh and aged cells with enough details to see difference of cooling system inputs and design. In the next subsection of results, the thermal runaway will be studied for both types of cells when one cell is triggered.

(a)   (b)

(c)   (d)
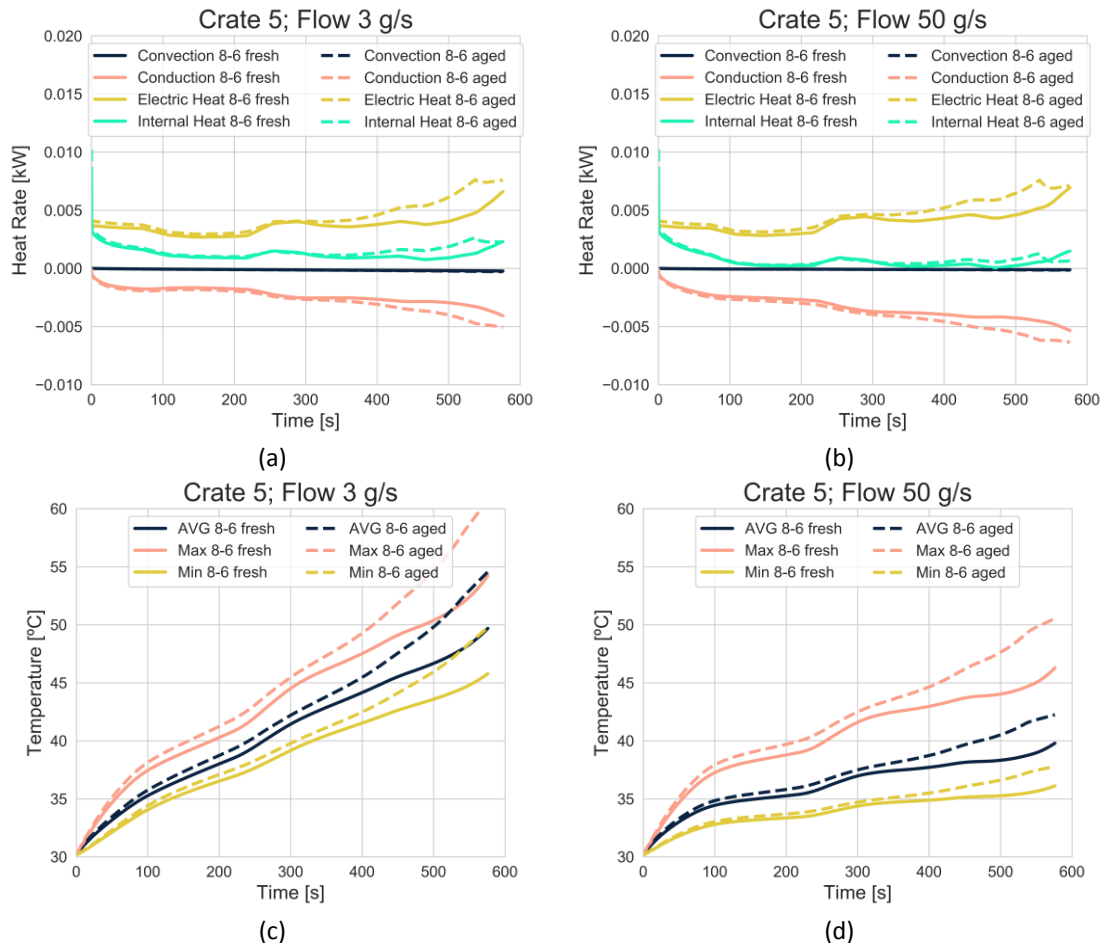
Figure 14 – Heat rate for cell 8-6 500 cycles aged and fresh when 5 Crate discharge is requested and the cooling flow is 3 g/s (a) and 50 g/s (b). The Average, Maximum and Minimum temperature for 3 g/s (c) and 50 g/s (d) is also presented.

3.3. Battery Thermal Runaway

As previously stated, the battery aging plays a significant role on the battery performance since it reduces the energy availability in the cell and enhances the heat generation due to increased internal resistance. Therefore, it is expected that the thermal runaway occurrence may be influenced by the aging, modifying both the time to start the process as well as its evolution. Therefore, both Kriston and Ren mechanisms were simulated considering the condition of low coolant flow (3 g/s) and environment temperature of 30°C for both fresh and aged conditions. The result of this investigation is presented in Figure 15. The first noticeable difference regards the time for thermal runaway occurrence predicted from each of the mechanisms. The mechanism proposed

by Kriston results in an advanced thermal runaway occurrence compared to Ren. Nonetheless, the temperature threshold to thermal runaway occurrence seems to be maintained, independently on the mechanism used. In addition, as it can be seen, the thermal runaway is impacted by the aging of the cell for both mechanisms. This is a direct consequence of the higher temperatures that are obtained with an aged cell, as previously discussed in section 3.2. Nonetheless, it is important to remark that the differences between the aged and fresh case in the Ren mechanism are enhanced because of the later thermal runaway occurrence. As shown, the differences in the peak temperature for the Ren mechanism [12] between aged and fresh cell are higher since it occurs later in time. In this sense, it is subjected to the higher heat generation of the aged battery, resulting in early BTR occurrence for the aged cell and higher temperature peaks than the fresh one. Finally, it is important to note that the Kriston mechanism has more detailed reactions for the solid electrolyte interface decomposition. This causes a different increase of the temperature for the aged cells than in the Ren mechanism. In particular, for the Kriston mechanism a progressive increase of the temperature from second 16 to the thermal runaway occurrence can be found, while no heat release (temperature increase) can be appreciated in the Ren mechanism before the thermal runaway occurrence.
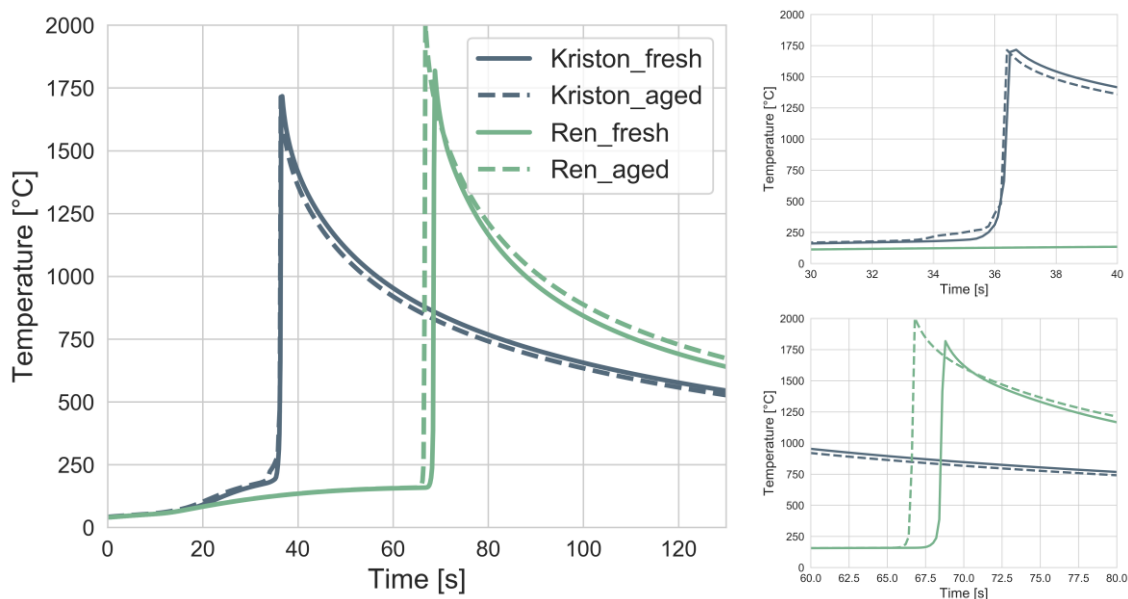
Figure 15 – Temperature evolution for the battery cell 8.5 considering both mechanism in a fresh cell and aged conditions (500 cycles).

Considering that the aged cases are critical for the thermal runaway occurrence, a detailed investigation was performed considering different flows (3 g/s and 20 g/s) and the impact that they may have on the heat transfer mechanism in the battery cell, the decomposition reaction, and the propagation of the battery thermal runaway for the remaining battery cells. Again, one of the battery cells (cell 8-6) is triggered by adding an experimentally measured heat release.

Figure 16 presents the evolution of the different element concentrations for each of the battery cells for the battery cell 8.5, considering both mechanisms and cooling mass flow

rates. As shown in Figure 16a (3 g/s), the mechanism differs largely on the evolution of the decomposition reactions as well as the time where they occur. For the Kriston mechanism [47], an early SEI decomposition is verified. Previous investigations have demonstrated that the Ren mechanism [12] have lower thermal runaway onset compared to the Kriston [47]. Nonetheless, it was also evidenced by the authors that the early reactions occur first for the Kriston mechanism [47]. In this sense, the SEI decomposition is aligned with the previous literature results. This allows to conclude that the energy released by the SEI decomposition can be the dominant effect on the thermal runaway occurrence.

In addition, it can be implied that the decomposition reactions modelled by the Kriston mechanism [47] occur in a much gradual way than those in the Ren mechanism [12]. While the last has an almost binary behavior, the former provides a gradual SEI decomposition. This indicates that the heat release occurs in a much broader temperature range, mainly for the initiation reactions, which may enhance the modelling of the conditions that leads to the abrupt temperature increased. It is also important to remark that while the 20 g/s cooling did no provided the activation energy for the Ren mechanism [12], low variations on the temperature threshold were verified with the Kriston mechanism [47]. This may also suggest that the last can guarantee safer design conditions compared to the former.

(a)   (b)
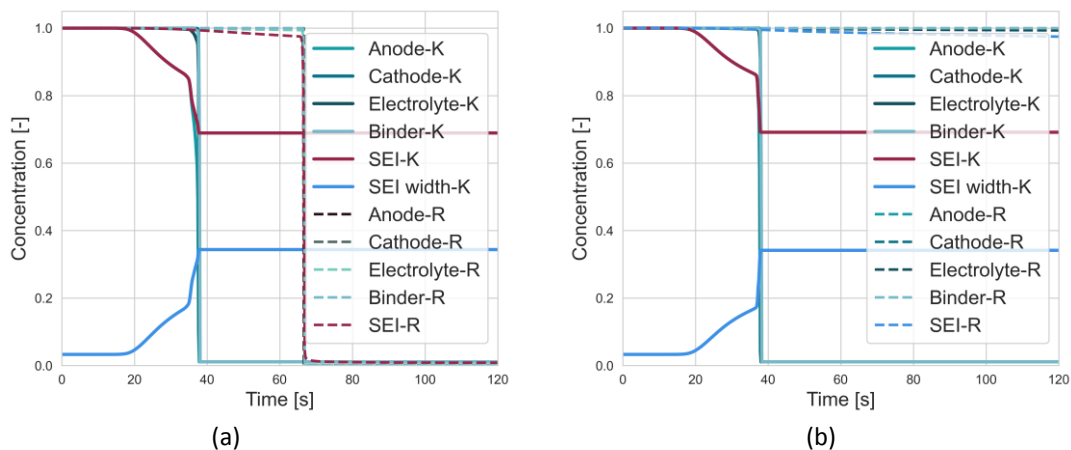
Figure 16 – Evolution of the components of the battery for both mechanisms (Kriston [47] and Ren [12]) for 3 g/s (a) and 20 g/s (b).

The thermal runaway will occur whenever the energy balance considering the heat generated by the decomposition reactions and Joule effect surpass the heat losses by conduction and convection to the cooling system and the environment. Therefore, the tracking of the different battery heat sources and sinks is an effective way to understand the differences observed between each mechanism and cooling mass flow rates. This is depicted in Figure 17 and Figure 18, where Figure 17a and Figure 17b presents the case with 3 g/s while Figure 18a and Figure 18b represents the case with 20 g/s. Considering the case of 3 g/s, it is evident that the heat released by the SEI decomposition plays a fundamental role on conditioning the temperature in favor of the thermal runaway occurrence. Despite that the SEI decomposition starts at similar temperature levels, or takes nearly the same time to starts, the amount of heat released is far different. For

the Kriston's mechanism [47], the heat released by the SEI decomposition can achieve as much as 1000 W while Ren's [12] has values of ≈ 80 W. This difference on the BTR heat release also modifies the conduction heat transfer behavior and shortens the time to achieve the decomposition of the cathode and anode, which are characterized by the fast increase in the temperature profiles, i.e., high exothermic reactions.
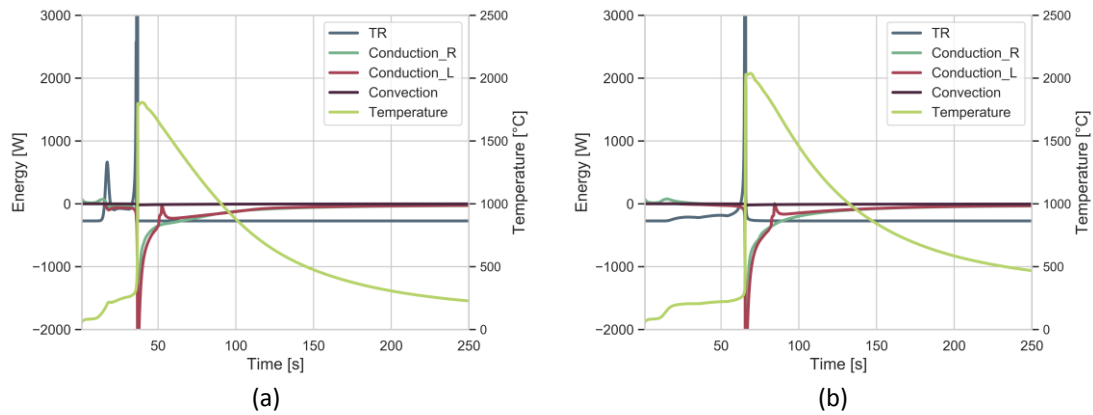

(a)   (b)

Figure 17 – Energy balance considering thermal runaway, conduction, and convection energy flows for Kriston [47] (a) and Ren [12] (b) mechanisms with a coolant mass flow rate of 3 g/s.

For the 20 g/s case (Figure 18), a similar behavior is evidenced for the Kriston mechanism [47], whereas Ren mechanism [12] is not able to sustain the decomposition reactions for long times. This can be justified again by the amount of energy released by the SEI. Both mechanisms depict a similar time where the SEI decomposition occurs, nonetheless, Ren's mechanism [12] heat release does not surpass the 50 W. This small temperature increase does not allow to activate the following decomposition reactions. In this sense, the battery cell continues to loss the heat to the cooling system, hindering the occurrence of thermal runaway.

(a)   (b)
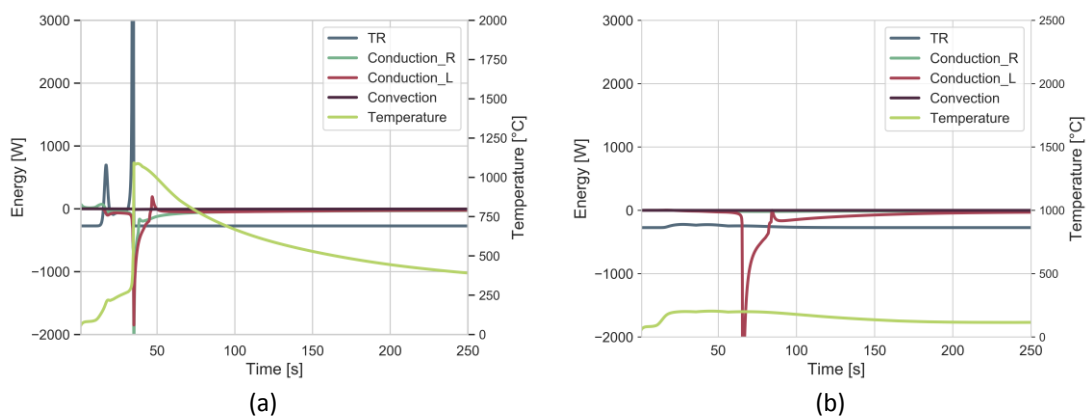
Figure 18 – Energy balance considering thermal runaway, conduction, and convection energy flows for Kriston [47] (a) and Ren [12] (b) mechanisms with a coolant mass flow rate of 20 g/s.

A global perspective of the thermal runaway occurrence is attempted by describing the time spent for each battery to enter in thermal runaway considering both mechanism and the 3 g/s of mass flow rate in the cooling system. Figure 19 summarizes the ignition delay time, defined as the time spent to reach the maximum derivative of the temperature signal and present the scheme of the 20 batteries that were evaluated to allow the tracking of the BTR evolution. As it can be evidenced, in general, the ignition

delay determination of each mechanism differs in approximately from 30 to 40 s. Despite the difference, it can be inferred that the predictive capability is still inside of the expected range. This is supported by the methodology that is used to develop this mechanism, which involves differential scanning calorimeter and accelerated rate calorimeter that have hours as order of magnitude in the assessments [46][45]. Therefore, differences in seconds and minutes are still acceptable.

It can be also highlighted that the propagation of thermal runaway occurs differently for both mechanisms of the cells near to the trigger cell are assessed. For example, while the Kriston mechanism [47] predicts that the cell 7.6 and cell 8.7 are the firsts to enter in BTR after the event is triggered in cell 8.6, the Ren mechanism [12] indicates that the cells 8.5 and 9.5 are the firsts to ignite. It is believed that the difference in the ignition sequence is highly dependent on the energy that is released at the low temperatures, i.e., during the SEI decomposition. From the previous analysis, it was evidenced that the Kriston mechanism releases much higher energies at low temperature values, which may lead to an overload of the heat transfer system at those conditions, igniting the vicinity cells.
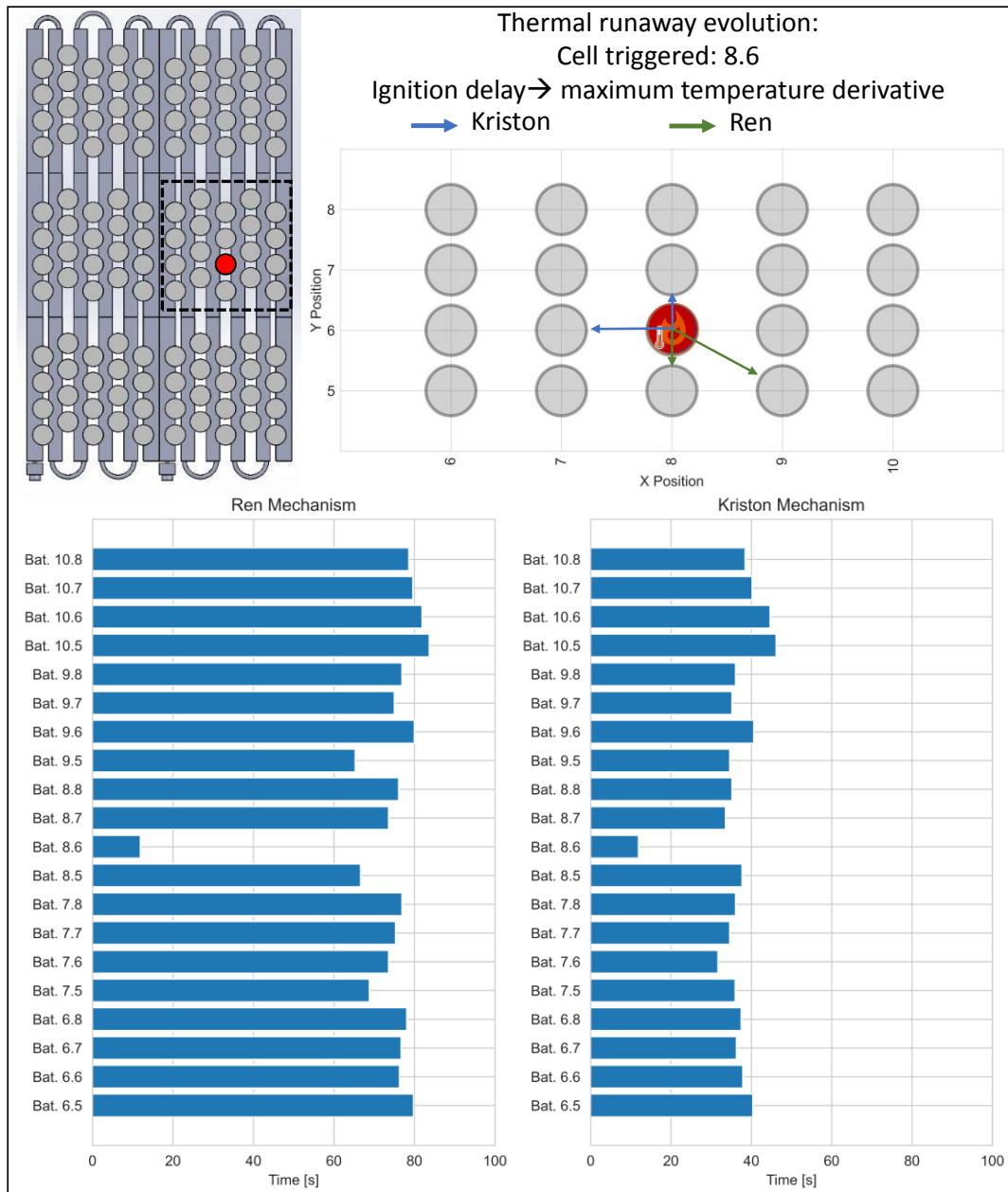
Figure 19 – Summary of the battery thermal runaway ignition delay for the 20 different battery cells considering both Kriston [47] and Ren mechanism [12] with a flow rate of 3 g/s.

Considering the battery cells disposition it can be argued that the solution using the Ren mechanism [12] depicts a more realistic scenario, indicating that the neighborhood cells with warmer flow conditions are the ones that are affected first by the heating of the cell 8.6. However, experimental investigations replicating the numerical experiment must be carried to validate these results. Despite this, the proposed framework is a valuable tool that enables the detailed investigation of BTR while considering the most important phenomena that occurs during the battery operation in normal and abuse conditions.

4. Conclusions

This work has proposed a novel framework for a coupled description of the cooling system and the most important phenomena that occurs during a Lithium-Ion battery operation such as degradation, SEI growth and lithium plating. The results allowed to conclude that the methodology can capture the instantaneous evolution of the main sinks and heat sources that affect the battery performance for fresh and aged conditions. The implementation of the battery thermal runaway kinetics mechanism from Ren et. al. [12] and Kriston et. al. [47] allowed also to compare the impact of the energy distribution on the thermal runaway propagation. From the results obtained, main conclusions can be drawn:

- The aging effects such as lithium plating and solid electrolyte interface growing must be included even if only heat transfer is considered, since these effects modifies the internal resistance and the associated heat generation from the cell.
- The combination of 0-D, 1-D and 3-D description for thermal runaway and electric circuit solution, flow modelling, and temperature distribution in the cell, respectively, is a powerful tool to model the multi-physics process involved in the battery operation.
- The framework can consider the particularities of each reaction kinetic mechanism and their impact on the BTR propagation.
- The aged cells shown more probabilities of thermal runaway due to the increase of the internal resistance. However, it is possible to reduce the difference by increasing the cooling flow from 3 g/s to 50 g/s.
- For 3 g/s of coolant flow the temperature variation is higher than 10°C. However, when the flow is increased the variation is reduced below ±2.5°C.
- The proper description of the early decomposition reactions is of utmost importance to provide detailed quantification of the thermal runaway onset. These reactions tend to compensate the heat losses to the cooling system and modify the slope of the temperature increase, advancing the BTR occurrence.
- Differences of approximately 30 s to 40 s were found between Ren [12] and Kriston [47] mechanism for the ignition delay. Additionally, Ren's mechanism [12] provided a more physical solution regarding the evolution of the thermal runaway process, indicating that the heat flows from the triggered cells to the vicinity.

In this sense, it can be argued that the framework is a suitable tool which provide the media to design battery modules and packs with reasonable accuracy. In addition, is possible to consider the most significant electrochemical and thermal effects that may affect battery performance. Additional investigations will be performed in future works to validate the methodology regarding the thermal runaway evolution by considering real battery modules and cooling systems.

Acknowledgments

References

[1]   A. García, J. Monsalve-Serrano, R. Sari, N. Dimitrakopoulos, M. Tunér, P. Tunestål, Performance and emissions of a series hybrid vehicle powered by a gasoline partially premixed combustion engine, Appl. Therm. Eng. 150 (2019). https://doi.org/10.1016/j.applthermaleng.2019.01.035.

[2]   V. Nimesh, R. Kumari, N. Soni, A.K. Goswami, V. Mahendra Reddy, Implication viability assessment of electric vehicles for different regions: An approach of life cycle assessment considering exergy analysis and battery degradation, Energy Convers. Manag. 237 (2021) 114104. https://doi.org/10.1016/j.enconman.2021.114104.

[3]   A. García, J. Monsalve-Serrano, S. Martinez-Boggio, P. Gaillard, O. Poussin, A.A. Amer, Dual fuel combustion and hybrid electric powertrains as potential solution to achieve 2025 emissions targets in medium duty trucks sector, Energy Convers. Manag. 224 (2020) 113320. https://doi.org/10.1016/j.enconman.2020.113320.

[4]   P. Olmeda, A. García, J. Monsalve-Serrano, R. Lago Sari, Experimental investigation on RCCI heat transfer in a light-duty diesel engine with different fuels: Comparison versus conventional diesel combustion, Appl. Therm. Eng. 144 (2018) 424–436. https://doi.org/10.1016/j.applthermaleng.2018.08.082.

[5]   S. Martinez, S. Merola, A. Irimescu, Flame Front and Burned Gas Characteristics for Different Split Injection Ratios and Phasing in an Optical GDI Engine, Appl. Sci. 9 (2019) 449. https://doi.org/10.3390/app9030449.

[6]   A. Peñaranda, S.D.D. Martinez Boggio, P.T.T. Lacava, S. Merola, A. Irimescu, Characterization of flame front propagation during early and late combustion for methane-hydrogen fueling of an optically accessible SI engine, Int. J. Hydrogen Energy. 43 (2018) 23538–23557. https://doi.org/10.1016/j.ijhydene.2018.10.167.

[7]   A. García, P. Carlucci, J. Monsalve-Serrano, A. Valletta, S. Martínez-Boggio, Energy management strategies comparison for a parallel full hybrid electric vehicle using Reactivity Controlled Compression Ignition combustion, Appl. Energy. 272 (2020) 115191. https://doi.org/10.1016/j.apenergy.2020.115191.

[8]   S. Ahmadi, S.M.T. Bathaee, A.H. Hosseinpour, Improving fuel economy and performance of a fuel-cell hybrid electric vehicle (fuel-cell, battery, and ultra-capacitor) using optimized energy management strategy, Energy Convers. Manag. 160 (2018) 74–84. https://doi.org/10.1016/j.enconman.2018.01.020.

[9]   J. Benajes, A. García, J. Monsalve-Serrano, S. Martínez-Boggio, Emissions

reduction from passenger cars with RCCI plug-in hybrid electric vehicle technology, Appl. Therm. Eng. 164 (2020) 114430. https://doi.org/10.1016/j.applthermaleng.2019.114430.

[10] E.E. Michaelides, Thermodynamics and energy usage of electric vehicles, Energy Convers. Manag. 203 (2020) 112246. https://doi.org/10.1016/j.enconman.2019.112246.

[11] M. Al-Zareer, I. Dincer, M.A. Rosen, A novel approach for performance improvement of liquid to vapor based battery cooling systems, Energy Convers. Manag. 187 (2019) 191–204. https://doi.org/10.1016/j.enconman.2019.02.063.

[12] D. Ren, X. Liu, X. Feng, L. Lu, M. Ouyang, J. Li, X. He, Model-based thermal runaway prediction of lithium-ion batteries from kinetics analysis of cell components, Appl. Energy. 228 (2018) 633–644. https://doi.org/10.1016/j.apenergy.2018.06.126.

[13] J. E, B. Zhang, Y. Zeng, M. Wen, K. Wei, Z. Huang, J. Chen, H. Zhu, Y. Deng, Effects analysis on active equalization control of lithium-ion batteries based on intelligent estimation of the state-of-charge, Energy. 238 (2022) 121822. https://doi.org/10.1016/j.energy.2021.121822.

[14] T. Katrašnik, I. Mele, K. Zelič, Multi-scale modelling of Lithium-ion batteries: From transport phenomena to the outbreak of thermal runaway, Energy Convers. Manag. 236 (2021). https://doi.org/10.1016/j.enconman.2021.114036.

[15] J. Deng, C. Bae, J. Marcicki, A. Masias, T. Miller, Safety modelling and testing of lithium-ion batteries in electrified vehicles, Nat. Energy. 3 (2018) 261–266. https://doi.org/10.1038/s41560-018-0122-3.

[16] Y. Chen, Y. Kang, Y. Zhao, L. Wang, J. Liu, Y. Li, Z. Liang, X. He, X. Li, N. Tavajohi, B. Li, A review of lithium-ion battery safety concerns: The issues, strategies, and testing standards, J. Energy Chem. 59 (2021) 83–99. https://doi.org/10.1016/j.jechem.2020.10.017.

[17] P. Liu, Y. Li, B. Mao, M. Chen, Z. Huang, Q. Wang, Experimental study on thermal runaway and fire behaviors of large format lithium iron phosphate battery, Appl. Therm. Eng. 192 (2021) 116949. https://doi.org/10.1016/j.applthermaleng.2021.116949.

[18] M. Malik, I. Dincer, M.A. Rosen, M. Mathew, M. Fowler, Thermal and electrical performance evaluations of series connected Li-ion batteries in a pack with liquid cooling, Appl. Therm. Eng. 129 (2018) 472–481. https://doi.org/10.1016/j.applthermaleng.2017.10.029.

[19] Y. Chung, M.S. Kim, Thermal analysis and pack level design of battery thermal management system with liquid cooling for electric vehicles, Energy Convers. Manag. 196 (2019) 105–116. https://doi.org/10.1016/j.enconman.2019.05.083.

[20] J. E, F. Yi, W. Li, B. Zhang, H. Zuo, K. Wei, J. Chen, H. Zhu, H. Zhu, Y. Deng, Effect analysis on heat dissipation performance enhancement of a lithium-ion-battery pack with heat pipe for central and southern regions in China, Energy. 226

(2021) 120336. https://doi.org/10.1016/j.energy.2021.120336.

[21] H. Zhang, C. Li, R. Zhang, Y. Lin, H. Fang, Thermal analysis of a 6s4p Lithium-ion battery pack cooled by cold plates based on a multi-domain modeling framework, Appl. Therm. Eng. 173 (2020) 115216. https://doi.org/10.1016/j.applthermaleng.2020.115216.

[22] Z. Liu, A. Ivanco, S. Onori, Aging characterization and modeling of nickel-manganese-cobalt lithium-ion batteries for 48V mild hybrid electric vehicle applications, J. Energy Storage. 21 (2019) 519–527. https://doi.org/10.1016/j.est.2018.11.016.

[23] K. Monika, C. Chakraborty, S. Roy, S. Dinda, S.A. Singh, S.P. Datta, Parametric investigation to optimize the thermal management of pouch type lithium-ion batteries with mini-channel cold plates, Int. J. Heat Mass Transf. 164 (2021). https://doi.org/10.1016/j.ijheatmasstransfer.2020.120568.

[24] J. Guo, F. Jiang, A novel electric vehicle thermal management system based on cooling and heating of batteries by refrigerant, Energy Convers. Manag. 237 (2021) 114145. https://doi.org/10.1016/j.enconman.2021.114145.

[25] J. Chen, S. Kang, J. E, Z. Huang, K. Wei, B. Zhang, H. Zhu, Y. Deng, F. Zhang, G. Liao, Effects of different phase change material thermal management strategies on the cooling performance of the power lithium ion batteries: A review, J. Power Sources. 442 (2019) 227228. https://doi.org/10.1016/j.jpowsour.2019.227228.

[26] F. Yi, J. E, B. Zhang, H. Zuo, K. Wei, J. Chen, H. Zhu, H. Zhu, Y. Deng, Effects analysis on heat dissipation characteristics of lithium-ion battery thermal management system under the synergism of phase change material and liquid cooling method, Renew. Energy. 181 (2022) 472–489. https://doi.org/10.1016/j.renene.2021.09.073.

[27] Z. Qian, Y. Li, Z. Rao, Thermal performance of lithium-ion battery thermal management system by using mini-channel cooling, Energy Convers. Manag. 126 (2016) 622–631. https://doi.org/10.1016/j.enconman.2016.08.063.

[28] X. Feng, X. He, M. Ouyang, L. Wang, L. Lu, D. Ren, S. Santhanagopalan, A Coupled Electrochemical-Thermal Failure Model for Predicting the Thermal Runaway Behavior of Lithium-Ion Batteries, J. Electrochem. Soc. 165 (2018) A3748–A3765. https://doi.org/10.1149/2.0311816jes.

[29] S. Hekmat, G.R. Molaeimanesh, Hybrid thermal management of a Li-ion battery module with phase change material and cooling water pipes: An experimental investigation, Appl. Therm. Eng. 166 (2020) 114759. https://doi.org/10.1016/j.applthermaleng.2019.114759.

[30] H. Zuo, B. Zhang, Z. Huang, K. Wei, H. Zhu, J. Tan, Effect analysis on SOC values of the power lithium manganate battery during discharging process and its intelligent estimation, Energy. 238 (2022) 121854. https://doi.org/10.1016/j.energy.2021.121854.

[31] Y. Liu, Y. Zhu, Y. Cui, Challenges and opportunities towards fast-charging battery materials, Nat. Energy. 4 (2019) 540–550. https://doi.org/10.1038/s41560-019-0405-3.

[32] A.W. Golubkov, S. Scheikl, R. Planteu, G. Voitic, H. Wiltsche, C. Stangl, G. Fauler, A. Thaler, V. Hacker, Thermal runaway of commercial 18650 Li-ion batteries with LFP and NCA cathodes - Impact of state of charge and overcharge, RSC Adv. 5 (2015) 57171–57186. https://doi.org/10.1039/c5ra05897j.

[33] John Newman, Electromechanical Systems, Third edit, University of California, Berkeley, 2004.

[34] A. Salvadori, D. Grazioli, M.G.D. Geers, Governing equations for a two-scale analysis of Li-ion battery cells, Int. J. Solids Struct. 59 (2015) 90–109. https://doi.org/10.1016/j.ijsolstr.2015.01.014.

[35] E.J.F. Dickinson, A.J. Wain, The Butler-Volmer equation in electrochemical theory: Origins, value, and practical application, J. Electroanal. Chem. 872 (2020) 114145. https://doi.org/10.1016/j.jelechem.2020.114145.

[36] Y. Gao, C. Zhu, X. Zhang, B. Guo, Implementation and evaluation of a practical electrochemical- thermal model of lithium-ion batteries for EV battery management system, Energy. 221 (2021) 119688. https://doi.org/10.1016/j.energy.2020.119688.

[37] BATEMO, batemo-cell-library/inr18650-20r, (n.d.).

[38] S.S. Zhang, K. Xu, T.R. Jow, Electrochemical impedance study on the low temperature of Li-ion batteries, Electrochim. Acta. 49 (2004) 1057–1061. https://doi.org/10.1016/j.electacta.2003.10.016.

[39] G. Nagasubramanian, Electrical characteristics of 18650 Li-ion cells at low temperatures, J. Appl. Electrochem. 31 (2001) 99–104. https://doi.org/10.1023/A:1004113825283.

[40] Y. Ji, Y. Zhang, C.-Y. Wang, Li-ion cell operation at low temperatures, J. Electrochem. Soc. 160 (2013) A636–A649. https://doi.org/10.1149/2.047304jes.

[41] GT-SUITE, AutoLion Application Manual and Calibration Procedure, (2020).

[42] S.F. Schuster, T. Bach, E. Fleder, J. Müller, M. Brand, G. Sextl, A. Jossen, Nonlinear aging characteristics of lithium-ion cells under different operational conditions, J. Energy Storage. 1 (2015) 44–53. https://doi.org/10.1016/j.est.2015.05.003.

[43] D. Ren, X. Feng, L. Lu, M. Ouyang, S. Zheng, J. Li, X. He, An electrochemical-thermal coupled overcharge-to-thermal-runaway model for lithium ion battery, J. Power Sources. 364 (2017) 328–340. https://doi.org/10.1016/j.jpowsour.2017.08.035.

[44] S. Bilyaz, K.C. Marr, O.A. Ezekoye, Modeling of Thermal Runaway Propagation in a Pouch Cell Stack, Fire Technol. 56 (2020) 2441–2466. https://doi.org/10.1007/s10694-020-00970-6.

[45] T.D. Hatchard, D.D. MacNeil, A. Basu, J.R. Dahn, Thermal Model of Cylindrical and Prismatic Lithium-Ion Cells, J. Electrochem. Soc. 148 (2001) A755. https://doi.org/10.1149/1.1377592.

[46] G.H. Kim, A. Pesaran, R. Spotnitz, A three-dimensional thermal abuse model for lithium-ion cells, J. Power Sources. 170 (2007) 476–489. https://doi.org/10.1016/j.jpowsour.2007.04.018.

[47] A. Kriston, I. Adanouj, V. Ruiz, A. Pfrang, Quantification and simulation of thermal decomposition reactions of Li-ion battery materials by simultaneous thermal analysis coupled with gas analysis, J. Power Sources. 435 (2019) 1–13. https://doi.org/10.1016/j.jpowsour.2019.226774.

[48] X. Feng, M. Ouyang, X. Liu, L. Lu, Y. Xia, X. He, Thermal runaway mechanism of lithium ion battery for electric vehicles: A review, Energy Storage Mater. 10 (2018) 246–267. https://doi.org/10.1016/j.ensm.2017.05.013.

[49] A. García, J. Monsalve-Serrano, R. Lago Sari, Á. Fogué Robles, Numerical analysis of kinetic mechanisms for battery thermal runaway prediction in lithium-ion batteries, Int. J. Engine Res. (2021) 146808742110299. https://doi.org/10.1177/14680874211029902.

[50] L. Zhang, P. Zhao, M. Xu, X. Wang, Computational identification of the safety regime of Li-ion battery thermal runaway, Appl. Energy. 261 (2020) 114440. https://doi.org/10.1016/j.apenergy.2019.114440.

[51] J. Xu, C. Lan, Y. Qiao, Y. Ma, Prevent thermal runaway of lithium-ion batteries with minichannel cooling, Appl. Therm. Eng. 110 (2017) 883–890. https://doi.org/10.1016/j.applthermaleng.2016.08.151.

[52] A. Bhattacharjee, R.K. Mohanty, A. Ghosh, Design of an Optimized Thermal Management System for Li-Ion Batteries under Different Discharging Conditions, Energies. 13 (2020) 5695. https://doi.org/10.3390/en13215695.

[53] P. Sun, R. Bisschop, H. Niu, X. Huang, A Review of Battery Fires in Electric Vehicles, Springer US, 2020. https://doi.org/10.1007/s10694-019-00944-3.

[54] J.B. Ferber, E. Straubel, D. Berdichevsky, T. Lyons, M. Colson, I. Eberhard, R. Wright, Battery mounting and cooling system, n.d. https://patents.google.com/patent/US20140178722A1/en.

[55] D. Bernardi, E. Pawlikowski, J. Newman, A General Energy Balance for Battery Systems, 132 (1985) 5–12. https://doi.org/10.1149/1.2113792.

[56] J. Kim, A. Mallarapu, D.P. Finegan, S. Santhanagopalan, Modeling cell venting and gas-phase reactions in 18650 lithium ion batteries during thermal runaway, J. Power Sources. 489 (2021) 229496. https://doi.org/10.1016/j.jpowsour.2021.229496.

[57] A. García, J. Monsalve-serrano, R.L. Sari, S. Martinez-boggio, An optical investigation of thermal runway phenomenon under thermal abuse conditions, Energy Convers. Manag. 246 (2021) 114663. https://doi.org/10.1016/j.enconman.2021.114663.

[58]   S. Ahmed, I. Bloom, A.N. Jansen, T. Tanim, E.J. Dufek, A. Pesaran, A. Burnham, R.B. Carlson, F. Dias, K. Hardy, M. Keyser, C. Kreuzer, A. Markel, A. Meintz, C. Michelbacher, M. Mohanpurkar, P.A. Nelson, D.C. Robertson, D. Scoffield, M. Shirk, T. Stephens, R. Vijayagopal, J. Zhang, Enabling fast charging – A battery technology gap assessment, J. Power Sources. 367 (2017) 250–262. https://doi.org/10.1016/j.jpowsour.2017.06.055.

[59]   P. By, I.R.A. Bloom, Extreme Fast Charging – a Battery Technology Gap, 2017.

Appendix

Appendix A

To reduce the computational time, a single cell was characterized in GT-AutoLion regarding open circuit voltages, dynamic usage, and aging. Once the cell was fully characterized, the GT-AutoLion model was reduced to RC circuit branches that allows to obtain similar performance while reducing the computational time in order of magnitudes. The reduction process consists of three steps. First, each case that is intended to be evaluated (aged and fresh cells) are submitted to a given discharge process to obtain the resistance, SOC and voltage curves. This phase is carried out with the GT- AutoLion cells. The outputs of this simulation are used as inputs for the second phase, which consists of characterizing an electrical equivalent circuit model (resistance, open circuit voltage, capacitance). Finally, a validation step is performed comparing the results obtained from simulation the complete GT-AutoLion model of the battery cell with that from the electric-equivalent model. These results are shown in Figure A1 and Figure A2. As it can be seen, both cases (fresh and aged cell s) are able to provide similar results for both modelling approaches, allowing to conclude that the simplified model is able to provide similar description of the relevant electrical characteristics of the battery cell.

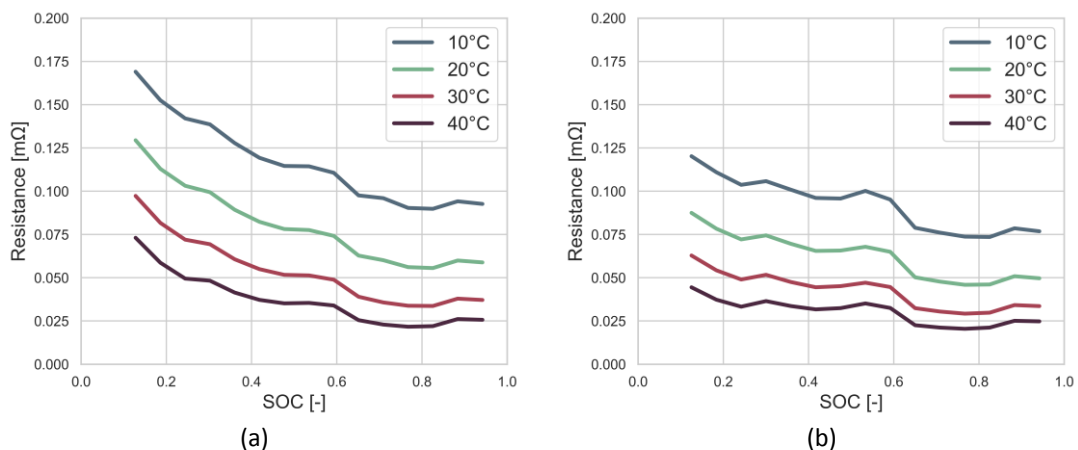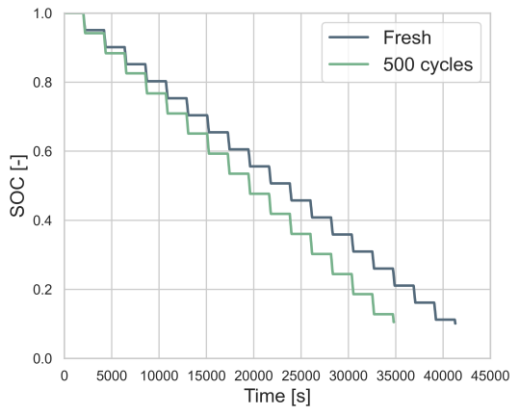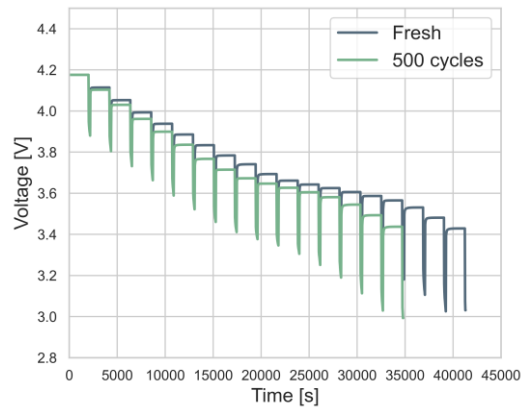(a)   (b)

Figure A1– Battery cell internal resistance for fresh(a) and 500 cycles aged (b) conditions and different cells temperatures (10 °C, 20 °C, 30 °C, 40 °C).
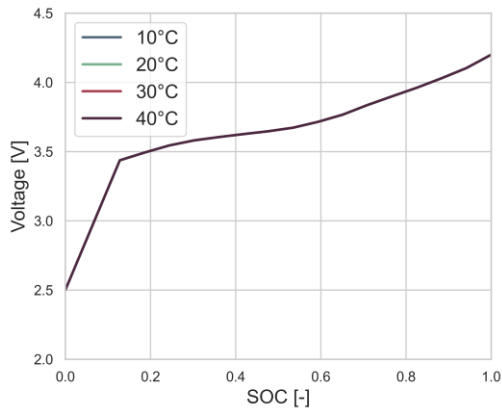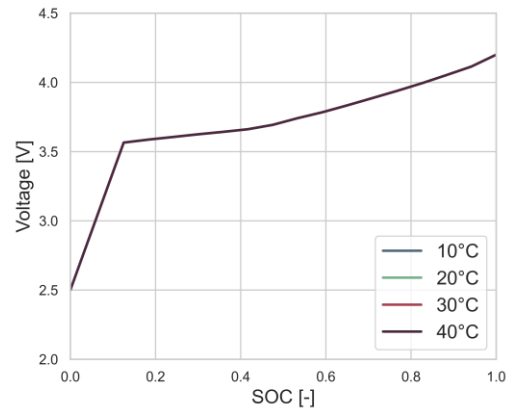
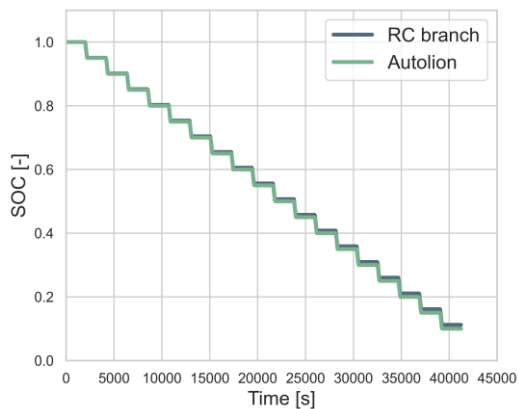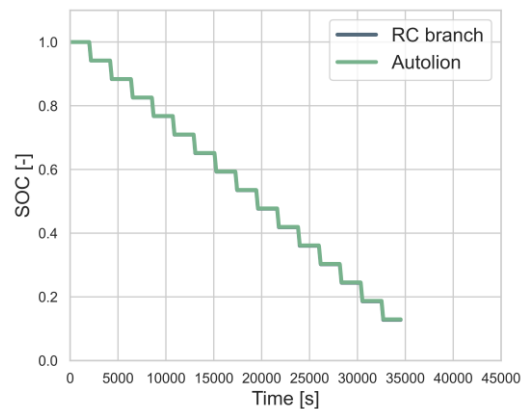Figure A2– State of Charge (a) and Voltage (b)for fresh and 500 cycles aged conditions.

Figure A3 – Open circuit voltages for fresh(a) and 500 cycles aged (b) conditions and different cells temperatures (10 oC, 20 oC, 30 oC, 40 oC).

Figure A4 – State of charge comparison between GT-Autolion cell and electric equivalent circuit for fresh cells (a) and aged cells with 500 cycles (b).
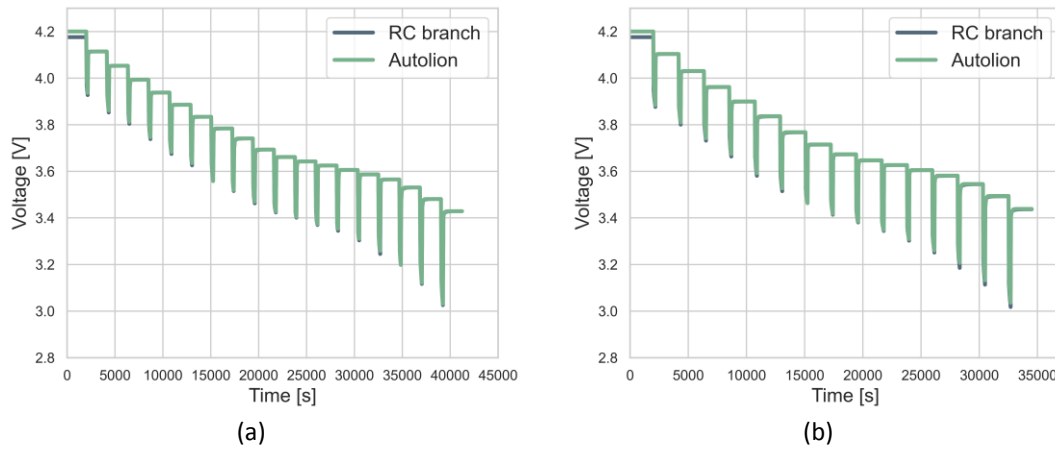
Figure A5 – Voltage comparison between GT-Autolion cell and electric equivalent circuit for fresh cells (a) and aged cells with 500 cycles (b).

Appendix B

The use of a finite element approach to determine the cell temperature distribution is highly dependent on the boundary conditions determination. In this sense, this appendix aims to illustrate which were the selections considered as the boundaries in the battery cell and the battery cooling plates. As it is shown in Figure B1, the battery is divided in three different parts. The first one consists of the cells domain that has no direct contact to the cooling. For this selection, the cell is exposed only to convective heat losses as a boundary condition (5 W/m²K), which is related to natural convection of air. Next, two additional selections are included that refers to both parts of the battery cell that are in contact with the cooling walls. The left- and right-hand side of the cell have the same contact are with each of the cooling channels. The boundary condition in this case is a conductive heat transfer with an equivalent conductive heat transfer coefficient of 10000 W/m²K.
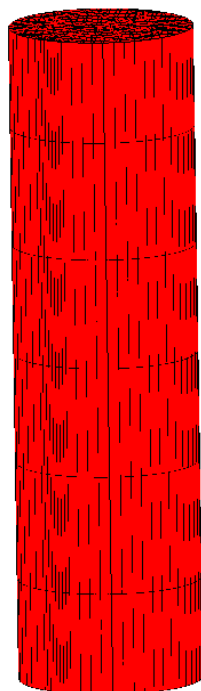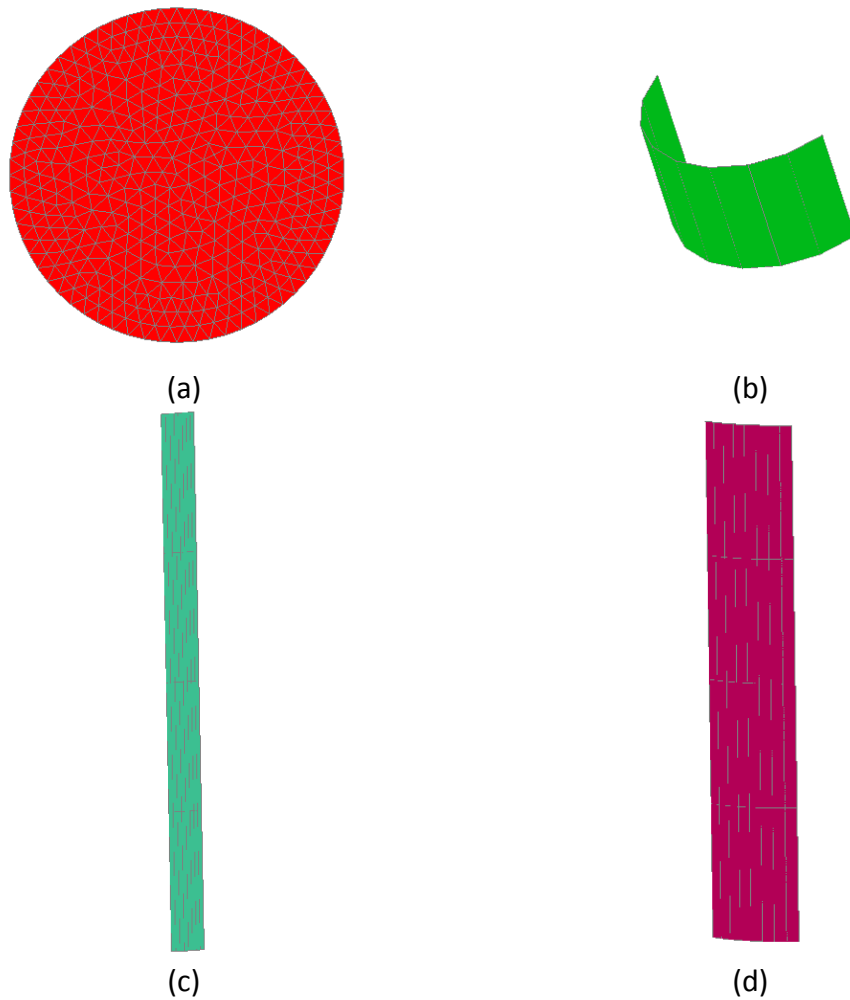
(a)

(b)

(c)

(d)

Figure B2 – Boundary conditions of the battery cell FE structure: top and bottom of the cell under convection heat transfer (a) lateral top and bottom under natural convection with ambient air (b), lateral center of the cell under natural convection with ambient air (c) and lateral center of the cell with contact of the cooling plate (d).

A similar approach is applied for the cooling system, dividing each part of the different walls in the respective boundary conditions. Except for the parts that are in contact with the battery, the remaining cooling walls have a convective heat transfer to the environment.

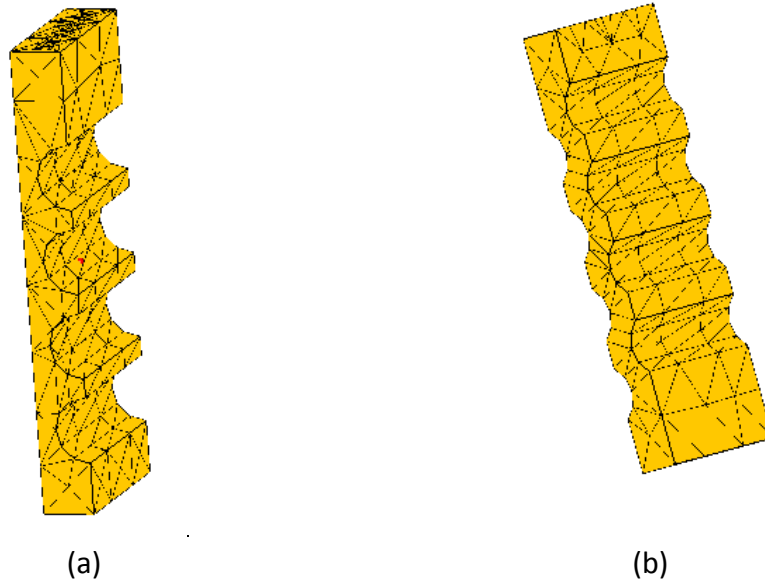(a)   (b)

Figure B3 – FE structure for the cooling system considering the external (a) and the internal walls (b).

The cell was studied with different size of mesh to see its influence on the temperature distribution. For speed up the process, a single battery cell was taken and study under known cooling conditions. The same battery cell of the study (electrical properties) with equal surface was taken. The natural convection is set with a h= 5 W/m²K and the ambient temperature at 30°C. The cell in contact with the cooling plates is set with a h= 1000 W/m²K and the fluid temperature of 25°C. The electric requirements are set with a constant current discharge of 5C and start SOC of 1.0. The results below show the cell with SOC 0.2 for two different mesh. It is possible to see that above 500 elements the results are maintained equal. Therefore, the case 3 (564 element) was chosen, since it offers a balance between computational requirement and accuracy.
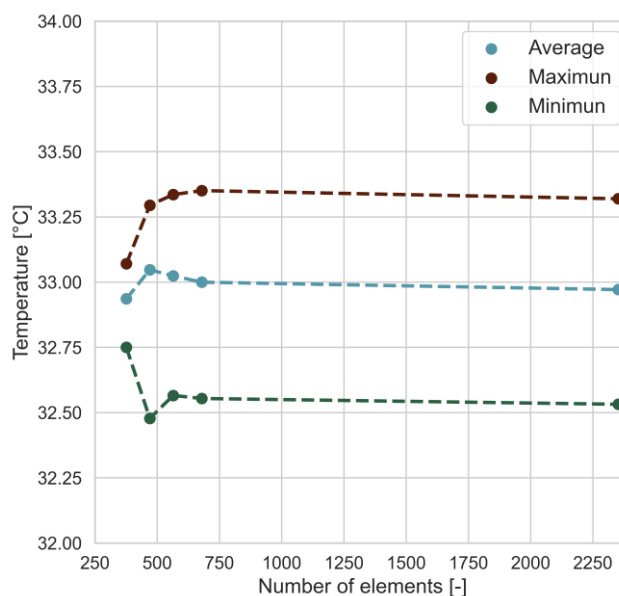

Figure B3 – Mesh independence study for the battery cell under controlled cooling conditions. Discharge rate 5C. starting with SOC 1.0. The instant where the temperature is showed represents to SOC 0.2.